Non-Probabilistic Uncertainty Quantification for Dynamic Characterization Functions Using Complex Ratio Interval Arithmetic Operation of Multidimensional Parallelepiped Model

Meng-Yun Zhao[1], Wang-Ji Yan*[2], Ka-Veng Yuen[2], Michael Beer[3,4,5]

[1] Department of Civil Engineering, Hefei University of Technology, Anhui, China

[2] State Key Laboratory of Internet of Things for Smart City and Department of Civil and Environmental Engineering, University of Macau, People's Republic of China

[3] Institute for Risk and Reliability, Leibniz Universität Hannover, Hannover, Germany

[4] Institute for Risk and Uncertainty and School of Engineering, University of Liverpool, UK

[5] International Joint Research Center for Engineering Reliability and Stochastic Mechanics, Tongji University, PR China

Abstract: Uncertainty quantification for the experimental estimations of dynamic characterization functions, including frequency response functions (FRFs) and transmissibility functions (TFs), is of practical importance in improving the robustness of the real applications of these functions for system identification and structural health monitoring. Interval analysis is an appealing tool for dealing with the uncertainties of engineering problems in which only the bounds of uncertain parameters are available. FRFs and TFs are complex-valued random variables. However, due to the negligence of the dependencies of complex-valued variables, the existing complex ratio interval arithmetic operation can be overly conservative. In this study, the polar representation of complex ratio numbers was extended to complex ratio polar intervals and a multidimensional parallelepiped (MP) interval model was introduced to accommodate the dependence between the numerator and the denominator. Based on the explicit expressions of the MP model through a dependence matrix, two new global extrema searching schemes with and without the regularization of the uncertainty domain of the MP model were proposed in order to derive the explicit formulas of the upper and lower bounds of the magnitudes and

phases of the FRFs and TFs. The new schemes were then applied to the uncertainty propagation for a numerically simulated beam and a bridge subjected to a single excitation. The results showed that the interval overestimation problem could be significantly alleviated by using the new complex-valued ratio interval arithmetic operation of the parallelepiped model.

Keywords: Frequency response function; transmissibility; interval analysis; complex interval division; parallelepiped model; structural health monitoring

*Corresponding author.
E-mail address: zmyhfut@163.com (M.Y. Zhao); wangjiyan@um.edu.mo (W.J. Yan); kvyuen@um.edu.mo (K.V. Yuen); beer@irz.uni-hannover.de (M. Beer)

1 Introduction

As shown in Fig. 1, the input-system-output model is viewed as the most fundamental component in the structural dynamics [1,2]. Frequency response functions (FRFs) and transmissibility functions (TFs) are commonly used to characterize the dynamics of a system. FRFs are mathematical representations of the relationship between inputs and outputs [3], while TFs are mathematical representations of the output-to-output relationships of a system [4]. As the most prevalent frequency-domain analysis tools, FRFs and TFs have been successfully applied in many fields such as structural damage detection [5-7], modal analysis [8-10], structural model updating [11,12], response reconstruction [13,14] and structural vibration control [15].

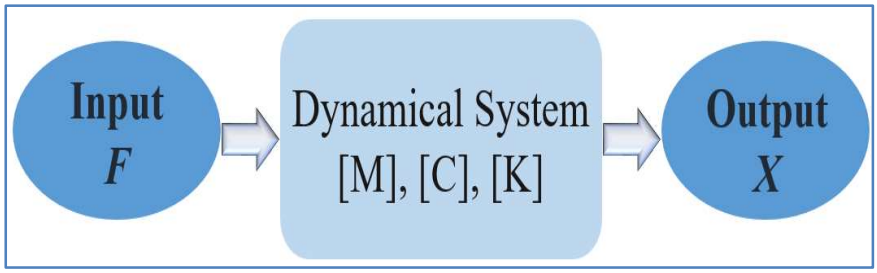

Fig. 1: Vibration-based system illustration composed of input, output, and a system model

The rationale behind the aforementioned applications is to make inferences about the parameters involved in a theoretical FRF model or TF model by fitting the theoretical FRF and TF models to their corresponding experimental models estimated from applied excitations and response measurements [16,17]. The experimental models of FRFs and TFs are estimated based on the Fourier transform of a time series, which is inevitably contaminated by different uncertainty sources such as the measurement noise, the inherent randomness of excitation, the numerical errors caused by discrete signals, and the variability of environmental conditions [18]. Therefore, the results of complex ratio functions obtained via deterministic analysis without considering randomness related to FFT coefficients can deviate substantially from the actual

values. As a result, quantification of the uncertainty for FRFs and TFs provides a rigorous solution for improving the robustness of real applications.

Many methods have emerged to quantify the uncertainty in engineering problems. These methods are generally categorized in two groups [19]: (i) probabilistic methods and (ii) non-probabilistic methods. The probabilistic methods are the most popular and fundamental methods for uncertainty quantification and propagation [20]. Over the past few years, different probabilistic approaches have been proposed to investigate the uncertainties of FRFs [21-23] and TFs [24-26]. However, in the context of limited, insufficient, vague, or ambiguous data, it is highly non-trivial to obtain the actual probability distribution because the prior estimation of the joint probability density function of the uncertain parameter values is subjective [27,28]. When a small number of experimental samples are available, the non-probabilistic convex model theory requiring to discern the uncertainty bounds instead of the probability distribution is deemed to be the most robust against data insufficiency since they are more objective with respect to the data [29,30]. For FFT coefficients, results have shown that for some frequency points, no regular probabilistic distribution is available even though the samples are sufficient [31]. In this regard, determining the bounds of a variable is a more straightforward and feasible alternative for uncertainty quantification than the identification of probability distributions.

Over the past few decades, interval analyses have been successfully applied in structural dynamics, such as computing the eigenvalue and eigenvector bounds of structures [32,33], calculation of envelope FRFs based on an interval finite element model [34,35], interval sensitivity analysis [36], response prediction [37], interval reliability analysis [38,39] and time-variant reliable control [40]. More recently, interval analyses have also gained widespread interests in inverse problems such as model updating [41] and dynamic load identification [42,43]. However, the interval quantization of the experimental estimation of FRFs and TFs

from measurements has not been established systematically, which has been attributed to the following challenges:

- FRFs and TFs are defined as the ratios of two frequency-domain responses, and they fall into the category of complex-valued ratio random variables. Although some complex-valued interval arithmetic operations have been proposed by a number of researchers [44,45], most complex-valued interval representations are somewhat complicated and they are not convenient for interval arithmetic operations.
- The FFT coefficients involved in FRFs or TFs are dependent. Direct use of the arithmetic operation rules based on a rectangular interval domain can lead to significant interval expansion, which affects the accuracy of uncertainty quantification significantly. Over the past few years, novel dependence analysis techniques such as the multidimensional ellipsoid model [46], multidimensional parallelepiped (MP) model [47], and copula pair construction [48] have been established for the non-probabilistic convex model by taking into account the independent and dependent interval variables in a unified framework. However, these models are still restricted to treating real-valued cases, and they have not been successfully applied in the interval analysis of a complex-valued domain.

To address the aforementioned difficulties, we aimed to extend the polar representation of complex ratio numbers to the case of interval ratio functions using the polar form [49]. As a result, the division of the complex interval analysis was converted into an interval division of two correlated magnitudes and an interval subtraction of two correlated angles. Subsequently, considering the fact that the MP model provided a potential solution for dependency problem, the MP model [50,51] was introduced in the context of a complex-valued interval ratio analysis to consider the dependence of the magnitudes (or phases) of the numerator and the denominator for the first time. Based on the novel expression of the MP model, two new schemes were

developed to solve the complex-valued ratio interval arithmetic operations: (1) A global extrema searching strategy in tandem with a regularization method to transform the MP model into a regular interval model, through which the uncertainty domain then became a multidimensional cube geometrically, and (2) a global extrema searching scheme for the MP model directly without the regularization of the uncertainty domain of the MP interval model. It is worth noting that the upper and lower bounds of the magnitude and phases of the FRFs and TFs could be derived explicitly for both schemes.

The organization of this paper is as follows. Section 2 formulates the background of this research. The fundamentals of the regular interval arithmetic as well as the complex-valued ratio interval variable with a polar form are introduced in Section 3. Section 4 describes the aim of accommodating the dependences involved in the complex ratio interval variable by introducing the novel development of MP model. Based on the explicit expressions of a parallelepiped model with a dependence matrix, two global extrema searching strategies with and without regularization of the uncertainty domain of the MP interval model were proposed in order to solve the complex-valued interval ratio arithmetic operation. The theoretical basis developments described in Section 3 and Section 4 were then utilized to compute the interval of the FRFs and TFs explicitly, as are discussed in Section 5. Finally, Section 6 describes how the two case studies were conducted to verify the theoretical developments.

2 Problem Description

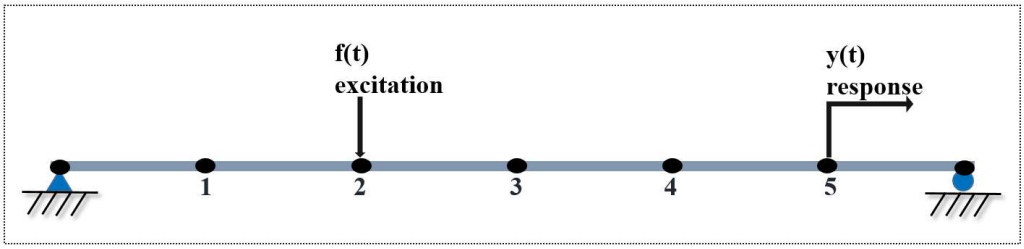

Fig. 2: Schematic diagram of a simply supported beam subjected to a single input

The multi-degree-of-freedom (MDOF) linear dynamical system shown in Fig. 2 was subjected to a single-input on the i-th DOF, and the response measurements were available for the n_o measured DOFs. The measurements of the input and outputs were denoted by $f_i(t)$ and $\mathbf{y}(t)=\left\{y_0(t),y_1(t),\cdots,y_{n_o}(t)\right\}^T$, respectively. At the frequency ω_k, the discrete Fourier transforms of the input and output measurements were defined as [52,53]:

$$F_i^{(k)}=F_i^{\Re}+\mathrm{i}F_i^{\Im}=\sqrt{\frac{\Delta t}{2\pi N}}\sum_{n'=0}^{N-1}f_i\left(n\Delta t\right)e^{\left(-\mathrm{i}\omega_k n\Delta t\right)} \tag{1a}$$

$$Y_j^{(k)}=Y_j^{\Re}+\mathrm{i}Y_j^{\Im}=\sqrt{\frac{\Delta t}{2\pi N}}\sum_{n'=0}^{N-1}y_j\left(n\Delta t\right)e^{\left(-\mathrm{i}\omega_k n\Delta t\right)} \tag{1b}$$

where $\omega_k=2\pi f_k$, $k=1,2,\cdots,Int(N/2)$, $\mathbf{i}^2=-1$, and $\Delta\omega=2\pi/(N\Delta t)$. In this work, '$\omega_k$' or superscript (k) denotes the k-th frequency point; $F_i^{(k)}$ and $Y_j^{(k)}$ were the discrete Fourier transforms of the input $f_i(t)$ and output $y_j(t)$ at ω_k, respectively; i and j denote the i-th DOF and j-th DOF of the system.

As a result, the FRF $H_{ij}^{(k)}$ reflecting the relationship between the input f_i and output y_i was defined as [3]:

$$H_{ij}^{(k)}=Y_j^{(k)}\Big/F_i^{(k)} \tag{2}$$

The TF $T_{ij}^{(k)}$ reflecting the relationship between a response y_j and y_i was defined as [4]:

$$T_{ij}^{(k)}=Y_j^{(k)}\Big/Y_i^{(k)} \tag{3}$$

As seen from Eqs. (2) and (3), both the FRFs and the TFs were complex-valued ratio random variables composed of both real and imaginary parts. Given some samples of the FFT pairs $\Psi_k=\left[F_i^{(k)},Y_j^{(k)}\right]$ or $\bar{\Psi}_k=\left[Y_i^{(k)},Y_j^{(k)}\right]$, which were possibly correlated with each other [54, 55], this study had the aim of quantifying the uncertainty of the FFT coefficients at different frequency points based on an MP model, which was subsequently used to explicitly quantify

the lower and upper bounds of the FRF and TF estimations $H_{ij}^{(k)}$ and $T_{ij}^{(k)}$ by developing new complex ratio interval arithmetic operations.

3 Complex-Valued Ratio Interval Variable with Polar Form

3.1 Fundamentals of the regular interval arithmetic

If $\underline{x}$ and $\overline{x}$ represent the lower and upper bounds of the interval variable X, then the standard interval model is given by [30]:

$$[x]=[\underline{x},\overline{x}]=\{x|\underline{x}\le x\le\overline{x}\} \tag{4}$$

The midpoint x^M and radius x^R of X are defined as:

$$x^M=(\underline{x}+\overline{x})/2 \tag{5a}$$

$$x^R=(\overline{x}-\underline{x})/2 \tag{5b}$$

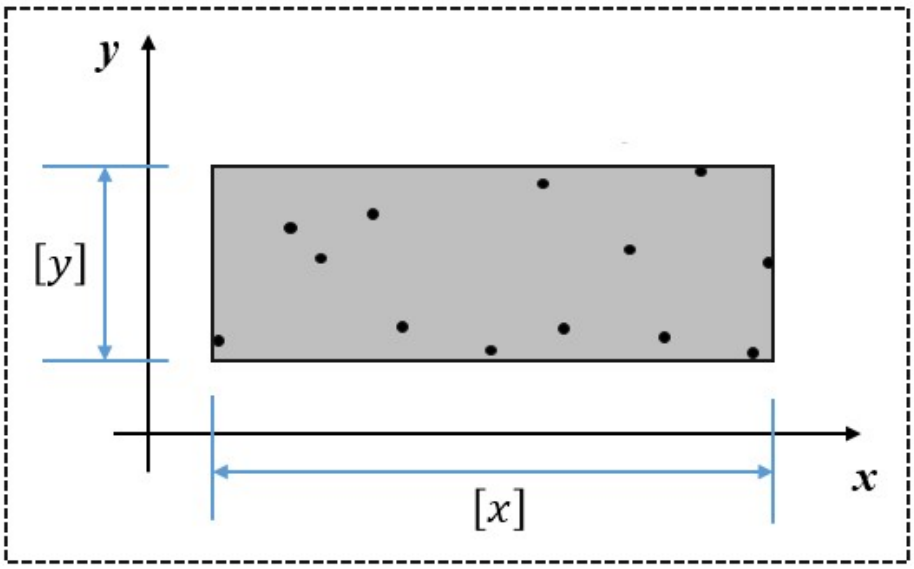

Fig. 3: Regular interval model for $[x]=[\underline{x},\overline{x}]$ and $[y]=[\underline{y},\overline{y}]$

Let $[x]=[\underline{x},\overline{x}]$ and $[y]=[\underline{y},\overline{y}]$ be real compact intervals as shown in Fig. 3. Without considering their dependences, the following rules hold for two independent interval variables

[30]:

$$[x]+[y]=\left[\underline{x}+\underline{y},\overline{x}+\overline{y}\right] \tag{6a}$$

$$[y]-[x]=\left[\underline{y}\text{-}\overline{x},\overline{y}\text{-}\underline{x}\right] \tag{6b}$$

$$[x]\bullet[y]=\left[\min\left(\underline{y}\,\underline{x},\underline{y}\,\overline{x},\overline{y}\,\underline{x},\overline{y}\,\overline{x}\right),\max\left(\underline{y}\,\underline{x},\underline{y}\,\overline{x},\overline{y}\,\underline{x},\overline{y}\,\overline{x}\right)\right] \tag{6c}$$

$$\frac{[y]}{[x]}=\left[\underline{y},\overline{y}\right]\times\left[\frac{1}{\overline{x}},\frac{1}{\underline{x}}\right],\ \text{if}\ 0\notin\left[\underline{x},\overline{x}\right] \tag{6d}$$

3.2 Polar complex intervals

Since FRFs and TFs have the same mathematical structure, for ease of illustration, they were denoted by a unified complex-valued ratio function $\mathcal{Z}$, denoted here using the polar form:

$$\mathcal{Z}=\frac{\chi_1}{\chi_2}=\frac{\rho_1 e^{\mathbf{i}\theta_1}}{\rho_2 e^{\mathbf{i}\theta_2}}=\frac{\rho_1}{\rho_2}e^{\mathbf{i}(\theta_1-\theta_2)} \tag{7}$$

where $\mathbf{i}=\sqrt{-1}$; χ_1 and χ_2 were two interval variables; the magnitude of $\mathcal{Z}$ was ρ_1/ρ_2, and the angle was $\theta_1-\theta_2$.

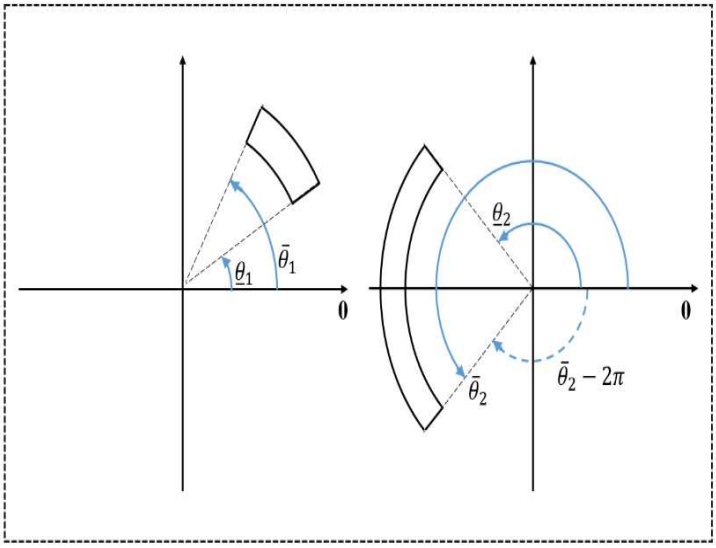

Fig. 4: Illustration of the choice of angles for sectors [49]

A polar interval model could be utilized to model the uncertainty of the FFT coefficients. As shown in Fig. 4, a polar interval model could be uniquely characterized by two real intervals, i.e., the magnitude and the phase:

$$[\rho_l]=\left[\underline{\rho_l},\overline{\rho_l}\right];\ \ [\theta_l]=\left[\underline{\theta_l},\overline{\theta_l}\right] \tag{8}$$

where the subscript l denotes the numerator or denominator.

Since all the angles were defined with modulo 2π, it was valid to adjust the angles by adding or subtracting 2π to their lower and upper bounds. In this study, the bounds of the angle interval of the denominator and numerator could be chosen such that:

$$\begin{cases} 0\le\underline{\theta_l}\le 4\pi;\ 0\le\overline{\theta_l}\le 4\pi, & \text{for } l\text{=numerator} \\ 0\le\underline{\theta_l}\le 2\pi;\ 0\le\overline{\theta_l}\le 2\pi, & \text{for } l\text{=denominator} \end{cases} \tag{9}$$

It is worth noting that the angle of the numerator should plus 2π if it is less than the angle of denominator the to avoid negative value of the phase of the complex-valued ratio variable and ensure it to fall into the interval of [0, 2π]. Therefore, the interval of a complex random variable was defined as [49]:

$$[\chi_l]=\left\{\chi_l\in\mathbb{C}\middle|\chi_l=\rho_l e^{\mathrm{i}\theta_l},\ \rho_l\in[\rho_l],\theta_l\in[\theta_l]\right\} \tag{10}$$

where $[\chi_l]$ was called a polar complex interval (or sector), which could also be denoted as $\left\{[\rho_l],[\theta_l]\right\}$.

Since the set of real intervals was closed with respect to subtraction and division, it could be seen that the division of the two sectors was also a sector:

$$[\mathcal{Z}]=\frac{[\chi_1]}{[\chi_2]}=\left\{\frac{[\rho_1]}{[\rho_2]},[\theta_1]-[\theta_2]\right\} \tag{11}$$

If the numerator and the denominator were independent, the magnitude and angle of the ratio interval variable could be calculated by utilizing the regular interval arithmetic:

$$[\rho_{\mathcal{Z}}]=\frac{[\rho_1]}{[\rho_2]}=\left[\underline{\rho_1},\overline{\rho_1}\right]\times\left[\frac{1}{\overline{\rho_2}},\frac{1}{\underline{\rho_2}}\right] \tag{12a}$$

$$[\theta_Z]=[\theta_1]-[\theta_2]=\left[\underline{\theta}_1-\bar{\theta}_2,\bar{\theta}_1-\underline{\theta}_2\right] \tag{12b}$$

where $0\notin\rho_2$.

However, in most applications, the numerator and the denominator were usually correlated. Due to the negligence of the dependencies of the complex-valued variables, the resultant intervals from the interval arithmetic were usually overestimated [51], and one could conclude this from the following examples.

Example 1 $\left([\rho_Z]=\dfrac{[\rho_1]}{[\rho_2]}\right)$: Assume that two variables ρ_1 and ρ_2 are correlated with $\rho_2=1+\rho_1$. The intervals are assumed to be $[\rho_1]=[2,3]$ and $[\rho_2]=[3,4]$. It is easily seen that the correct interval of ρ_Z is $\left[\frac{2}{3},\frac{3}{4}\right]$, but the result based on Eq. (12a) is $\left[\frac{1}{2},1\right]$.

Example 2 $\left([\theta_Z]=[\theta_1]-[\theta_2]\right)$: Assume that two variables θ_1 and θ_2 are correlated with $\theta_2=\frac{1}{2}\theta_1-\frac{\pi}{2}$. The intervals are $[\theta_1]=[\pi,2\pi]$ and $[\theta_2]=\left[0,\frac{\pi}{2}\right]$. Then, the correct interval of θ_Z is $\left[\pi,\frac{3\pi}{2}\right]$, which is different from the result $\left[\frac{\pi}{2},2\pi\right]$ from Eq. (12b).

From these two simple examples, it is clear that the interval arithmetic evaluation as an enclosure of the range over interval variables is dependent on the dependences between the two interval variables. To improve the accuracy, the MP interval model [50, 51] will be adopted to quantify the complex ratio interval variables and it will be introduced in the next section.

4 Complex-Valued Ratio Interval Arithmetic with the MP Model

4.1 Review of the MP interval model [50, 51]

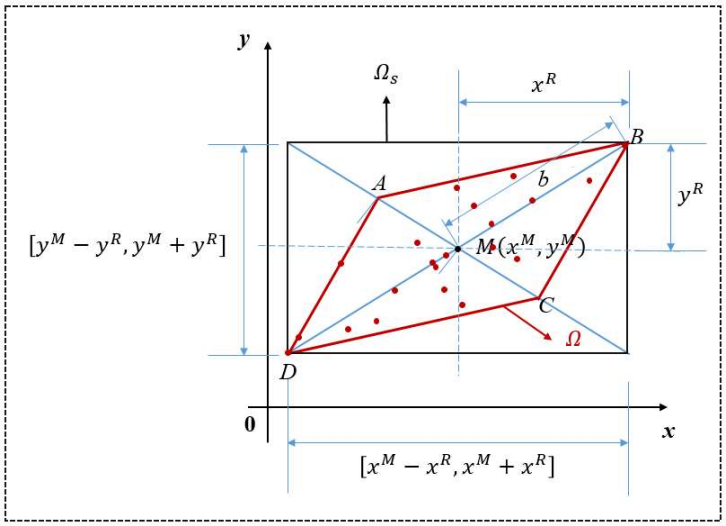

Fig. 5: Schematic diagram of the two-dimensional MP interval model (2-D case) [51]

For a two-dimensional case with interval variables X and Y, the schematic diagram of the MP model is shown in Fig. 5. In this model, the range of X and Y were denoted by $[x]=[x^M-x^R,x^M+x^R]$ and $[y]=[y^M-y^R,y^M+y^R]$, respectively. If X and Y were dependent, the uncertainty domain of the samples could be encompassed by a parallelogram domain Ω, while the joint uncertainty domain of X and Y constituted a rectangular domain Ω_s if X and Y were independent with each other. The uncertainty domain in the MP model was established according to the following principles: (a) The parallelogram Ω was circumscribed by the rectangular domain Ω_s, (b) The vertices of the parallelogram were located on the diagonal lines of Ω_s, (c) The parallelogram degenerated into a rectangular domain Ω_s, if and only if the interval variables X and Y were independent.

From the above principles, it was not difficult to deduce that the shape of the parallelogram should reflect the dependence between X and Y. The shape coefficient φ_{xy} between X

and Y was defined as follows:

$$\varphi_{xy}=\varphi_{yx}=\varphi=\frac{b-a}{b+a} \tag{13}$$

where a and b denote the semi-axis length in the directions $\overrightarrow{MB}$ and $\overrightarrow{MA}$, respectively.

It is worth mentioning here that, the MP model adopted in this study is different from the work by Elishakoff [56]. For MP model used in this study, the minimum-area rectangular circumscribing all data points should be determined at first, and then the parallelogram can be formulated automatically according to the principles mentioned in the above by using the diagonal lines. One advantage of the principles is that the shape of the parallelogram can reflect the dependence degree between X and Y, and it is easy to define the dependence coefficient φ_{xy} between X and Y based on the diagnonal lines. However, in Elishakoff's approach [56], one should seek for an optimal enclosing parallelogram which has one of the edges or along an edge of the convex hull. In a particular case that is parallel to two specific edges of the convex hull, and would coincide with above two edges of the convex hull. Following this, one can choose a parallelogram with at least two adjacent sides of it constitute sides of the convex hull, not necessarily adjacent. Then one proceeds with reducing the size of the parallelogram until the other sides of it contain at least one corner of the convex hull. As is indicated in Fig. 6, the four vertices of the parallelogram constructed by this method are not necessarily located on the diagonal of the circumscribed rectangle, and the shape coefficient and matrix transformation in MP are not suitable for the Elishakoff's parallelogram model again.

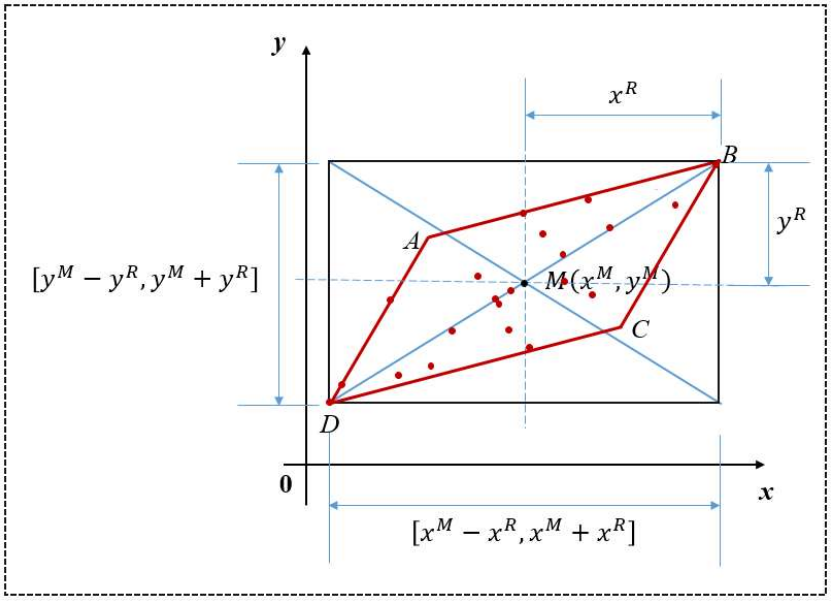

Fig. 6: Schematic diagram of the interval model constructed by Elishakoff [56]

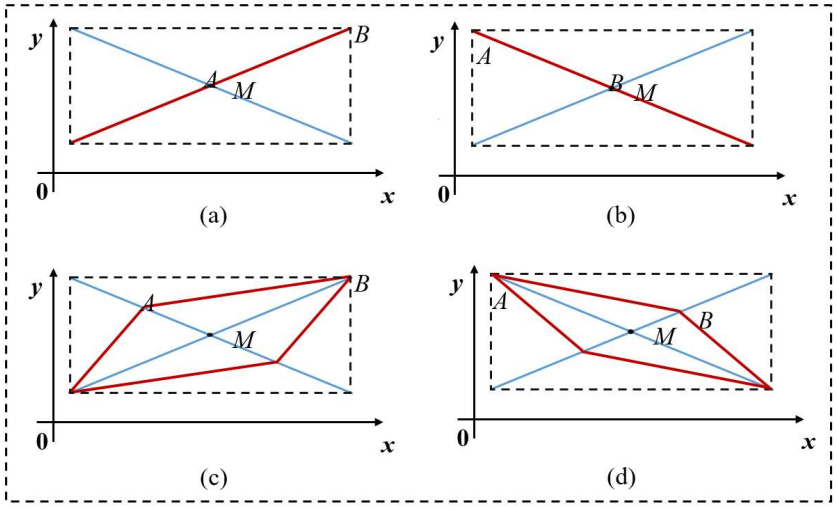

Fig. 7: Some cases between two interval variables for the MP model with different shape coefficients : (a) $\varphi = 1$; (b) $\varphi = -1$; (c) $0 < \varphi < 1$; (d) $-1 < \varphi < 0$ [50,51]

As is shown in Fig. 7(a) and 7(b), $\varphi = 1$ or $\varphi = -1$ when the interval variables X and Y had a linear dependence; when the interval variables X and Y had positive or negative dependences, $0 < \varphi < 1$ or $-1 < \varphi < 0$ (see Fig. 7(c) and 7(d)). The MP model degraded into a traditional interval model when the intervals were independent with $\varphi = 0$. Subsequently, the

symmetrical dependence matrix $\mathbf{\Phi}$ was defined as [50]:

$$\mathbf{\Phi}=\begin{bmatrix}\varphi_{xx} & \varphi_{xy}\\ \varphi_{yx} & \varphi_{yy}\end{bmatrix}=\begin{bmatrix}1 & \varphi\\ \varphi & 1\end{bmatrix} \tag{14}$$

Based on the above principles, an explicit expression of the uncertainty domain could be constructed in the following elementwise inequality:

$$-\boldsymbol{\eta}\le\mathbf{\Phi}^{-1}\mathbf{\Gamma}^{-1}\mathbf{H}^{-1}\begin{pmatrix}x & x-x^{M}\\ y & y-y^{M}\end{pmatrix}\le\boldsymbol{\eta} \tag{15}$$

where $\boldsymbol{\eta}=(1,1)^{T}$, and the matrices $\mathbf{\Gamma}$ and $\mathbf{H}$ were defined as:

$$\mathbf{\Gamma}=\begin{bmatrix}w_1 & 0\\ 0 & w_2\end{bmatrix}\ \text{with}\ w_i=\left(\sum_{j=1}^{2}\left|\mathbf{\Phi}(i,j)\right|\right)^{-1}\ (i=1,2) \tag{16a}$$

$$\mathbf{H}=\begin{bmatrix}x^{R} & 0\\ 0 & y^{R}\end{bmatrix} \tag{16b}$$

where $|\bullet|$ denotes the absolute value of each element in the vector. In the expression, $\mathbf{\Phi}(i,j)$ is the element in the i-th row and the j-th column of the dependence matrix $\mathbf{\Phi}$. By expanding Eq. (15), the description of the parallelogram turned out to be:

$$\begin{pmatrix}-1\\ -1\end{pmatrix}\le\begin{bmatrix}\dfrac{x^{R}}{1+|\varphi|} & \dfrac{\varphi x^{R}}{1+|\varphi|}\\ \dfrac{\varphi y^{R}}{1+|\varphi|} & \dfrac{y^{R}}{1+|\varphi|}\end{bmatrix}^{-1}\begin{pmatrix}x & x-x^{M}\\ y & y-y^{M}\end{pmatrix}\le\begin{pmatrix}1\\ 1\end{pmatrix} \tag{17}$$

Based on Eq. (17), the coordinates of the four vertices of this parallelogram (Nodes A, B, C, and D in Fig. 5) could be derived as [51]:

$$\begin{aligned}&A\left(x^{M}+\frac{-1+\varphi}{1+|\varphi|}x^{R},y^{M}+\frac{1-\varphi}{1+|\varphi|}y^{R}\right);\ B\left(x^{M}+\frac{1+\varphi}{1+|\varphi|}x^{R},y^{M}+\frac{1+\varphi}{1+|\varphi|}y^{R}\right)\\ &C\left(x^{M}+\frac{1-\varphi}{1+|\varphi|}x^{R},y^{M}+\frac{-1+\varphi}{1+|\varphi|}y^{R}\right);\ D\left(x^{M}+\frac{-1-\varphi}{1+|\varphi|}x^{R},y^{M}+\frac{-1-\varphi}{1+|\varphi|}y^{R}\right)\end{aligned} \tag{18}$$

Given some samples of $X^{(n)}$ and $Y^{(n)}$ $(n=1,2,\ldots,N_m)$, the MP model quantifying the domain of the uncertain variables could be constructed efficiently. The procedure for building the MP

model for the 2-D case is summarized as follows:

- The marginal intervals $[x]=\left[x^M-x^R, x^M+x^R\right]$ and $[y]=\left[y^M-y^R, y^M+y^R\right]$ were obtained.
- A minimum-area parallelogram enveloping all the samples $\left(X^{(n)}, Y^{(n)}\right)$ $n=1,2,\ldots,N_m$ was established.
- The dependence matrix $\mathbf{\Phi}$ was constructed using Eq. (13).
- The shape matrix $\mathbf{C}=\mathbf{H\Gamma\Phi}$ was constructed based on the obtained marginal intervals and the dependence matrix $\mathbf{\Phi}$.
- The uncertainty domains of X and Y were created from the coordinates of the four vertices of this parallelogram (Nodes A, B, C, and D in Fig. 5).

4.2 Two schemes for the complex ratio interval arithmetic operations

Based on the explicit expression of the MP model in terms of the dependence matrix, two schemes were proposed, as described in this section, including the global extrema searching strategy with regularization of the uncertainty domain as well as another strategy without regularization of the uncertainty domain. Since the interval analysis was used to estimate the lower and upper bounds of the function, the interval arithmetic could be transformed to compute the maximum and the minimum of $f(x,y)=\dfrac{y}{x}$ and $g(x,y)=y-x$.

4.2.1 The scheme with regularization of the uncertainty domain

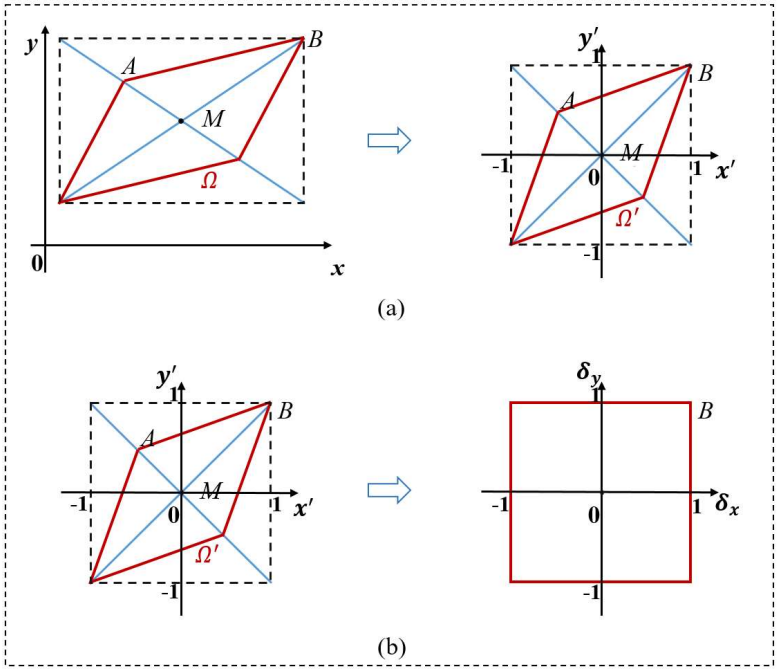

Fig. 8: Regularization of the uncertainty domain: (a) translation and compression transformation; (b) normalization transformation [51].

As is shown in Fig. 8, the regularization of the uncertainty domain was achieved through two stages [51].

(i) Translation and compression transformation

As is shown in Fig. 8(a), after the translation and scaling transformations, a new interval vector was obtained:

$$\Upsilon'=\begin{Bmatrix} x' \\ y' \end{Bmatrix}=\begin{bmatrix} x^R & 0 \\ 0 & y^R \end{bmatrix}^{-1}\begin{Bmatrix} x-x^M \\ y-y^M \end{Bmatrix} \tag{19}$$

After matrix transformation, the uncertainty domain became $\Omega'=\left\{\Upsilon'\left|\boldsymbol{\Phi}^{-1}\boldsymbol{\Gamma}^{-1}\Upsilon'\right|\le\boldsymbol{\eta}\right\}$ with $\boldsymbol{\eta}=(1,1)^T$.

(ii) Normalization transformation

As shown in Fig. 8(b), the domain was transformed into a standard multidimensional cuboid

with the midpoints of $\mathbf{0}$ and the semi-lengths of $\mathbf{1}$ by introducing a new vector $\boldsymbol{\delta}$:

$$\boldsymbol{\delta}=\begin{Bmatrix}\delta_x\\ \delta_y\end{Bmatrix}=\left(\begin{bmatrix}w_1 & 0\\ 0 & w_2\end{bmatrix}\begin{bmatrix}1 & \varphi\\ \varphi & 1\end{bmatrix}\right)^{-1}\begin{Bmatrix}x'\\ y'\end{Bmatrix} \tag{20}$$

where $[\delta_x]=[-1,1]$ and $[\delta_y]=[-1,1]$. As a result, the following expression could be obtained from Eqs. (19) and (20):

$$x=\frac{x^R}{\sum_{j=1}^{2}\left|\boldsymbol{\Phi}(1,j)\right|}\delta_x+\frac{x^R}{\sum_{j=1}^{2}\left|\boldsymbol{\Phi}(1,j)\right|}\varphi_{xy}\delta_y+x^M \tag{21a}$$

$$y=\frac{y^R}{\sum_{j=1}^{2}\left|\boldsymbol{\Phi}(2,j)\right|}\varphi_{xy}\delta_x+\frac{y^R}{\sum_{j=1}^{2}\left|\boldsymbol{\Phi}(2,j)\right|}\delta_y+y^M \tag{21b}$$

As a result, the regular interval operations considering the dependences of the variables could be achieved, as follows [51]:

$$\frac{[y]}{[x]}=\frac{y^M}{x^M}+\frac{\left(y^R-\frac{y^M}{x^M}\varphi x^R\right)[\delta_x]+\left(y^R\varphi-\frac{y^M}{x^M}x^R\right)[\delta_y]}{x^R\left(\varphi[\delta_x]+[\delta_y]\right)+x^M\left(1+|\varphi|\right)},\ 0\notin[\underline{x},\overline{x}] \tag{22a}$$

$$[y]-[x]=\frac{\varphi y^R-x^R}{1+|\varphi|}[\delta_x]+\frac{y^R\varphi-x^R}{1+|\varphi|}[\delta_y]+y^M-x^M \tag{22b}$$

where $[\delta_x]=[-1,1]$ and $[\delta_y]=[-1,1]$.

Since many effective methods had been previously developed for dealing with the regular interval model, they could be directly applied to the MP model after regularization. The subsequent uncertainty propagation analysis would become straightforward. However, by using Eq. (22a), interval overestimation occurred due to the multiple occurrences of δ_x and δ_y in the expressions. The multiple occurrences of δ_x and δ_y were regarded as multiple independent variables and this phenomenon induced the inherent defect of classic interval arithmetic.

To avoid interval overestimation, the interval arithmetic $\frac{[y]}{[x]}$ was transformed to compute the maximum and the minimum of the function $f(\delta_x,\delta_y)$ in terms of δ_x and δ_y:

$$f(\delta_x,\delta_y)=\frac{y}{x}=\frac{y^M}{x^M}+\frac{\left(y^R-\frac{y^M}{x^M}\varphi x^R\right)\delta_x+\left(y^R\varphi-\frac{y^M}{x^M}x^R\right)\delta_y}{x^R(\varphi\delta_x+\delta_y)+x^M(1+|\varphi|)},\ \delta_x\in[-1,1];\delta_y\in[-1,1] \tag{23}$$

The global maximum and minimum of $f(\delta_x,\delta_y)$ with respect to δ_x, δ_y were given by:

$$\begin{cases}\dfrac{\partial f(\delta_x,\delta_y)}{\partial\delta_x}=\dfrac{\left[x^Ry^R(1-\varphi^2)\right]\delta_y+(1+|\varphi|)(x^My^R-\varphi x^Ry^M)}{\left[x^R(\varphi\delta_x+\delta_y)+x^M(1+|\varphi|)\right]^2}=0\\ \dfrac{\partial f(\delta_x,\delta_y)}{\partial\delta_y}=\dfrac{\left[x^Ry^R(\varphi^2-1)\right]\delta_x+(1+|\varphi|)(x^My^R\varphi-x^Ry^M)}{\left[x^R(\varphi\delta_x+\delta_y)+x^M(1+|\varphi|)\right]^2}=0\end{cases} \tag{24}$$

Solving the above equations led to:

$$\begin{cases}\hat{\delta}_x=\dfrac{(1+|\varphi|)(\varphi x^My^R-x^Ry^M)}{x^Ry^R(1-\varphi^2)}\\ \hat{\delta}_y=\dfrac{(1+|\varphi|)(\varphi x^Ry^M-x^My^R)}{x^Ry^R(1-\varphi^2)}\end{cases} \tag{25}$$

It is worth noting that:

$$A=\frac{\partial^2 f(\delta_x,\delta_y)}{\partial\delta_x^2}=0;\ B=\frac{\partial^2 f(\delta_x,\delta_y)}{\partial\delta_x\delta_y}=0;\ C=\frac{\partial^2 f(\delta_x,\delta_y)}{\partial\delta_y^2}=0 \tag{26}$$

where A, B and C denote the second-order partial derivatives of $f(\delta_x,\delta_y)$ with respect to δ_x and δ_y. Eq.(26) satisfies $AC-B^2=0$, indicating that this was an optimization problem in a bounded domain. Therefore, the obtained extrema (which possibly did not exist) of $\frac{y}{x}$ had to be further compared with the values at the boundaries (the square in Fig. 8). It was not difficult to prove that $f(\delta_x,\delta_y)$ was a monotonic function at the boundaries, and the maximum and

minimum values at the boundaries occurred at four vertices. Therefore, $\frac{[y]}{[x]}$ could be evaluated as:

$$\frac{[y]}{[x]}=\left[\min\left(f(\pm1,\pm1),f\left(\hat{\delta}_x,\hat{\delta}_y\right)\right),\max\left(f(\pm1,\pm1),f\left(\hat{\delta}_x,\hat{\delta}_y\right)\right)\right] \tag{27}$$

where $f\left(\hat{\delta}_x,\hat{\delta}_y\right)$ could be obtained by substituting Eq. (25) into Eq. (23); $f(\pm1,\pm1)$ were the results estimated at four vertices.

Similarly, the interval arithmetic $[y]-[x]$ shown in Eq. (22b) could be transformed to compute the maximum and the minimum of the function $g\left(\hat{\delta}_x,\hat{\delta}_y\right)$ in terms of δ_x and δ_y:

$$g\left(\delta_x,\delta_y\right)=y-x=\frac{\varphi y^R-x^R}{1+|\varphi|}\delta_x+\frac{y^R-\varphi x^R}{1+|\varphi|}\delta_y+y^M-x^M,\ \delta_x\in[-1,1];\delta_y\in[-1,1] \tag{28}$$

The global maximum and minimum of $g\left(\delta_x,\delta_y\right)$ with respect to δ_x, δ_y were given by the following equations:

$$\begin{cases}\dfrac{\partial g\left(\delta_x,\delta_y\right)}{\partial\delta_x}=\dfrac{\varphi y^R-x^R}{1+|\varphi|}=0\\[2ex]\dfrac{\partial g\left(\delta_x,\delta_y\right)}{\partial\delta_y}=\dfrac{y^R-\varphi x^R}{1+|\varphi|}=0\end{cases} \tag{29}$$

Eq. (29) indicates that the equation had no solution, implying that $g\left(\delta_x,\delta_y\right)$ it was a monotonic function. Therefore, the interval of $[y]-[x]$ could be obtained through optimization at four vertices:

$$[y]-[x]=\left[\min\left(g(\pm1,\pm1)\right),\max\left(g(\pm1,\pm1)\right)\right] \tag{30}$$

4.2.2 The scheme without regularization of the uncertainty domain

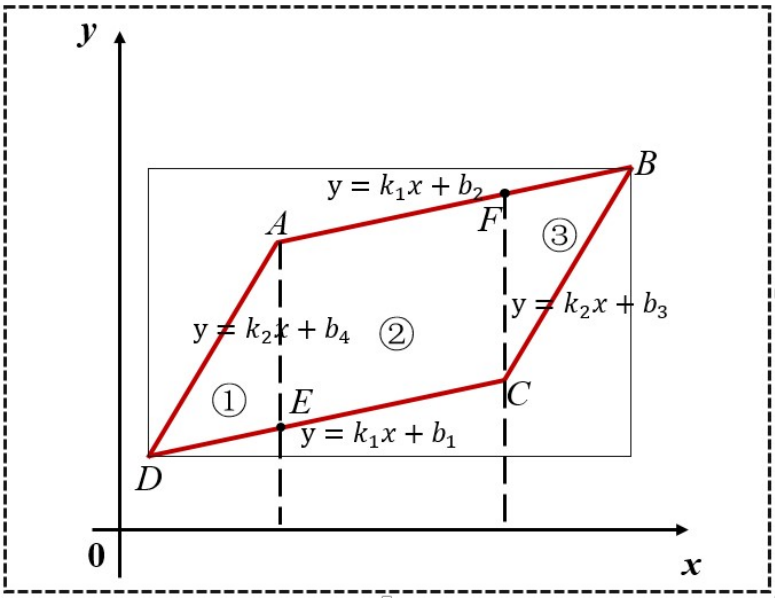

Fig. 9: Explicit expressions of the four sides of the MP model.

By revisiting the MP model without regularization of uncertainty domain shown in Fig. 9, the opposite sides of the parallelogram are in parallel. The expressions of the four lines including CD, AB, BC and AD are given by:

$$y_{CD}=k_1x+b_1;\ \ y_{AB}=k_1x+b_2;\ \ y_{BC}=k_2x+b_3;\ \ y_{AD}=k_2x+b_4 \tag{31}$$

where k_1 denotes the slope of lines CD and AB; and k_2 denotes the slope of lines BC and AD; b_1, b_2, b_3 and b_4 represent the corresponding vertical intercepts. Assume that the coordinates of the vertices are denoted by $A(x_A,y_A)$, $B(x_B,y_B)$, $C(x_C,y_C)$ and $D(x_D,y_D)$, then the slopes k_1 and k_2 of four sides of the MP interval model can be expressed as:

$$k_1=\frac{y_B-y_A}{x_B-x_A}=\frac{\varphi y^M}{x^M} \tag{32a}$$

$$k_2=\frac{y_B-y_C}{x_B-x_C}=\frac{y^M}{\varphi x^M} \tag{32b}$$

It is worth mentioning here that x^M and y^M denote the midpoints of interval variables X and Y, respectively. As a result, the intercepts of the four sides of the MP interval model shown in Fig. 9 are given by:

$$b_1 = y_D - k_1 x_D = y^M + \frac{-1-\varphi}{1+|\varphi|} y^R - \frac{\varphi y^R}{x^R}\left(x^M + \frac{-1-\varphi}{1+|\varphi|} x^R \right) \tag{33a}$$

$$b_2 = y_A - k_1 x_A = y^M + \frac{1-\varphi}{1+|\varphi|} y^R - \frac{\varphi y^R}{x^R}\left(x^M + \frac{-1+\varphi}{1+|\varphi|} x^R \right) \tag{33b}$$

$$b_3 = y_B - k_2 x_B = y^M + \frac{1+\varphi}{1+|\varphi|} y^R - \frac{y^R}{\varphi x^R}\left(x^M + \frac{1+\varphi}{1+|\varphi|} x^R \right) \tag{33c}$$

$$b_4 = y_A - k_2 x_A = y^M + \frac{1-\varphi}{1+|\varphi|} y^R - \frac{y^R}{\varphi x^R}\left(x^M + \frac{-1+\varphi}{1+|\varphi|} x^R \right) \tag{33d}$$

Based on the explicit expressions of Eqs. (32) and (33), the interval arithmetic is transformed to compute the maximum and the minimum of four lines CD, AB, BC and AD. One can prove that the interval operation can be achieved as:

$$\frac{[y]}{[x]} = \left[\min\left(\frac{y_A}{x_A}, \frac{y_B}{x_B}, \frac{y_C}{x_C}, \frac{y_D}{x_D} \right), \max\left(\frac{y_A}{x_A}, \frac{y_B}{x_B}, \frac{y_C}{x_C}, \frac{y_D}{x_D} \right) \right] \tag{34a}$$

$$\begin{aligned} [y]-[x] = \big[& \min\left(y_A - x_A, y_B - x_B, y_C - x_C, y_D - x_D \right), \\ & \max\left(y_A - x_A, y_B - x_B, y_C - x_C, y_D - x_D \right) \big] \end{aligned} \tag{34b}$$

The proofs are referred to Appendix A.

It is noted that the MP model is only a first rough approach to address dependencies between intervals, being used for illustrative purpose in the presentation of our method. For more complex and nonlinear problems we refer to model order reduction to facilitate the applicability of the MP model in those cases as well. Alternatively, for full scale analysis, more advanced dependency models can be implemented in our approach. For example, complicated dependence structures can be accommodated through copula pair construction approaches as

proposed by Faes and Moens in [48], where dependencies between intervals within an FE model are described in this manner. In [57] an error term is proposed to collect the contributions of nonlinear effects to account for nonlinear dependencies. Those are readily available for tailored implementation in dependence on the specific problem.

5 Uncertainty Quantification for FRFs and TFs based on new Schemes

In the context of interval analysis for FRF and TFs, the FFT coefficients $\Psi_k=\left[F_i^{(k)},Y_j^{(k)}\right]$ or $\bar{\Psi}_k=\left[Y_i^{(k)},Y_j^{(k)}\right]$ could be expressed using a polar form as:

$$F_i^{(k)}=\beta_i^{(k)}e^{\mathrm{i}\alpha_i^{(k)}};\quad Y_i^{(k)}=\rho_i^{(k)}e^{\mathrm{i}\theta_i^{(k)}};\quad Y_j^{(k)}=\rho_j^{(k)}e^{\mathrm{i}\theta_j^{(k)}} \tag{35}$$

where $\beta_i^{(k)}$ and $\alpha_i^{(k)}$ denote the magnitude and the phase of $F_i^{(k)}$, respectively; $\rho_i^{(k)}$ and $\theta_i^{(k)}$ denote the magnitude and angle of $Y_i^{(k)}$, respectively.

The polar interval model introduced in Section 3 could be utilized to model the uncertainty of the FFT coefficients. $F_i^{(k)}$, $Y_i^{(k)}$ and $Y_j^{(k)}$ could be uniquely characterized by the real intervals of $\left[\beta_i^{(k)}\right]=\left[\underline{\beta_i}^{(k)},\overline{\beta}_i^{(k)}\right]$, $\left[\alpha_i^{(k)}\right]=\left[\underline{\alpha_i}^{(k)},\overline{\alpha}_i^{(k)}\right]$, $\left[\rho_i^{(k)}\right]=\left[\underline{\rho_i}^{(k)},\overline{\rho}_i^{(k)}\right]$, $\left[\theta_i^{(k)}\right]=\left[\underline{\theta_i}^{(k)},\overline{\theta}_i^{(k)}\right]$, $\left[\rho_j^{(k)}\right]=\left[\underline{\rho_j}^{(k)},\overline{\rho}_j^{(k)}\right]$ and $\left[\theta_j^{(k)}\right]=\left[\underline{\theta_j}^{(k)},\overline{\theta}_j^{(k)}\right]$. As a result, the intervals of the FRFs and TFs were denoted by:

$$\left[H_{ij}^{(k)}\right]=\frac{\left[Y_j^{(k)}\right]}{\left[F_i^{(k)}\right]}=\left\{\frac{\left[\rho_j^{(k)}\right]}{\left[\beta_i^{(k)}\right]},\left[\theta_j^{(k)}\right]-\left[\alpha_i^{(k)}\right]\right\} \tag{36a}$$

$$\left[T_{ij}^{(k)}\right]=\frac{\left[Y_j^{(k)}\right]}{\left[Y_i^{(k)}\right]}=\left\{\frac{\left[\rho_j^{(k)}\right]}{\left[\rho_i^{(k)}\right]},\left[\theta_j^{(k)}\right]-\left[\theta_i^{(k)}\right]\right\} \tag{36b}$$

The intervals of the divisions of the FRFs and TFs $\left[\rho_j^{(k)}\right]/\left[\beta_i^{(k)}\right]$ and $\left[\rho_j^{(k)}\right]/\left[\rho_i^{(k)}\right]$ could be determined with Eq. (27) or Eq. (34a), while the subtractions $\left[\theta_j^{(k)}\right]-\left[\alpha_i^{(k)}\right]$ and

$\left[\theta_j^{(k)}\right]-\left[\theta_i^{(k)}\right]$ could be obtained using Eq. (30) or Eq. (34b). The procedures for computing the interval for the experimental estimation of the FRFs using the scheme with or without regularization of the uncertainty domain are summarized in Table 1. These procedures could be easily extended to the interval analysis for the TFs. However, these procedures have been omitted here for the purpose of simplicity.

Table 1: Interval analysis for the FRFs using the schemes with and without regularization of the uncertainty domain

Step	Procedures
1	Acquire the time histories of input $f_i(t)$ and output $y_j(t)$ of the dynamical system
2	Use Fourier transform for the time histories to obtain the samples of $[F_i^{(k)}, Y_j^{(k)}]^T$
3	Decide the marginal intervals of $[\beta_i^{(k)}]$, $[\alpha_i^{(k)}]$, $[\rho_i^{(k)}]$ and $[\theta_i^{(k)}]$ according to the upper and lower bounds of the magnitude and angle intervals
4	Analyze the interval of FRF within a specific frequency band $[\omega_{k_1}, \omega_{k_2}]$: FOR $k = k_1 : k_2$ ● Generate the two-dimensional parallelogram model circumscribed by the rectangular domain; ● Compute the shape coefficients of $[\beta_i^{(k)}]$ & $[\rho_i^{(k)}]$, $[\alpha_i^{(k)}]$ & $[\theta_i^{(k)}]$; ● Calculate $[\rho_j^{(k)}]/[\beta_i^{(k)}]$ according to Eq. (27) or Eq. (34a); ● Calculate $[\theta_j^{(k)}]-[\alpha_i^{(k)}]$ according to Eq. (30) or Eq. (34b); END FOR

6 Case Studies

6.1 Numerical study of a simply supported beam

Simulated data of a simply supported beam, as shown in Fig. 2, was processed to illustrate the accuracy of the proposed interval analysis schemes for experimentally estimated FRFs and TFs. The length was 3 m and the cross section was 100 mm$\times 20$ mm (width × height), the Young's modulus was $E=7\times10^{10}$ Pa, the density was $\rho=2760$ kg/m^3, and the damping ratios for the first two modes were $\varsigma_1=\varsigma_2=1\%$ for the Rayleigh damping model. Random excitation was applied

at sensor 2, as shown in Fig. 2. The response measurements were assumed to be contaminated by Gaussian white noise. We know that signal-to-noise-ratio (SNR) is defined as the ratio of the noise-free signal power to the noise power expressed in dB. The SNR level of this example was assumed to be 50 dB in this study. The time histories were generated to verify the proposed approaches. One hundred realizations, each with a duration of 50*s* were generated for both the noise-free and noise-contaminated scenarios with a sampling time interval $\Delta t = 0.02\text{s}$. The FFT coefficients were calculated for each realization of the input and output. The interval analysis for the FRFs and TFs could be conducted by following the procedures shown in Table 1.

The FRF corresponding to the fifth floor and the first floor ($H_{2,1}^{(k)}$) at $w_k = 12.2\pi$ rad/s was observed in detail by taking the ratio of $X_1^{(k)}$ to $F_1^{(k)}$ directly without averaging, smoothing, windowing, etc. The marginal intervals of the magnitudes and angles could be obtained as $[\beta_2^{(k)}]=[0.5744, 21.91]$, $[\rho_1^{(k)}]=[0.1266, 3.586]$, $[\alpha_2^{(k)}]=[0.04081, 6.243]$, and $[\theta_1^{(k)}]=[0.3952, 12.1]$ according to the samples of the FFT coefficients. The MP model of $[\beta_2^{(k)}]$ and $[\rho_1^{(k)}]$, as well as $[\alpha_2^{(k)}]$ and $[\theta_1^{(k)}]$ could be generated by circumscribing all of the samples. The shape coefficient of $[\beta_2^{(k)}]$ and $[\rho_1^{(k)}]$ was equal to $\varphi_k = 0.73$, while the shape coefficient of $[\alpha_2^{(k)}]$ and $[\theta_1^{(k)}]$ was equal to $\varphi_k = 0.32$. The parallelograms fitting the measured data in the two-dimensional spaces are illustrated in Fig. 10(a) and 10(b). It could be observed that the parallelograms were thin and long, implying that both the pairs of random variables $\left(\beta_2^{(k)}, \rho_1^{(k)}\right)$ and $\left(\alpha_2^{(k)}, \theta_1^{(k)}\right)$ were significantly correlated with each other. The parallelepiped model had good fitting for the 100 samples. Based on this uncertainty domain, uncertainty quantitation could then be carried out for the FRFs at different frequency points. Fig. 11(a) displays the intervals of the magnitude of $H_{2,1}^{(k)}$ (i.e., $[\rho_1^{(k)}]/[\beta_2^{(k)}]$) which was computed according to Eq. (27) and Eq. (34a) within the frequency band of [0,25]Hz. Fig. 11(b) shows the intervals of the

angles of $H_{2,1}^{(k)}$ (i.e., $[\theta_1^{(k)}]-[\alpha_2^{(k)}]$) that were achieved using Eqs. (30) and (34b). For the comparison purpose, the intervals of $[\rho_1^{(k)}]/[\beta_2^{(k)}]$ and $[\theta_1^{(k)}]-[\alpha_2^{(k)}]$ without considering the dependence degree computed using Eqs. (6d) and (6b) were also determined, as shown in Fig. 11(a) and (b). The figure also includes the result of $[\rho_1^{(k)}]/[\beta_2^{(k)}]$ that was computed using Eq.(22a) as well as the results of $[\theta_1^{(k)}]-[\alpha_2^{(k)}]$ that were computed using Eq. (22b), which were originally derived in [51].

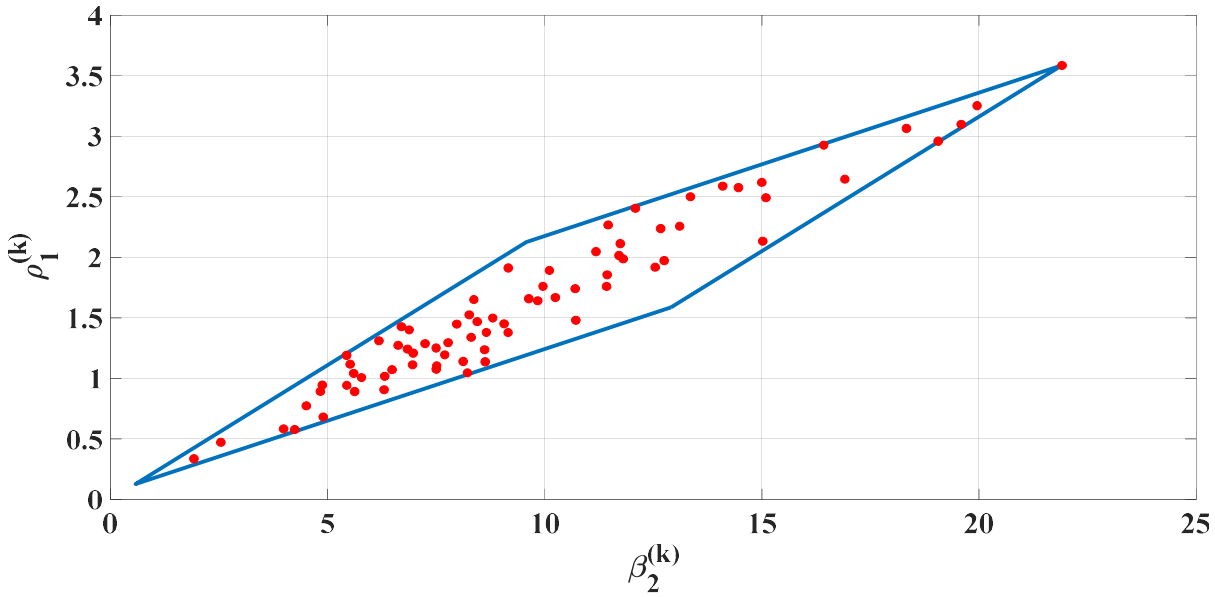

(a) $\left(\beta_2^{(k)}, \rho_1^{(k)}\right)$ at $\omega_k = 12.2\pi$ rad/s

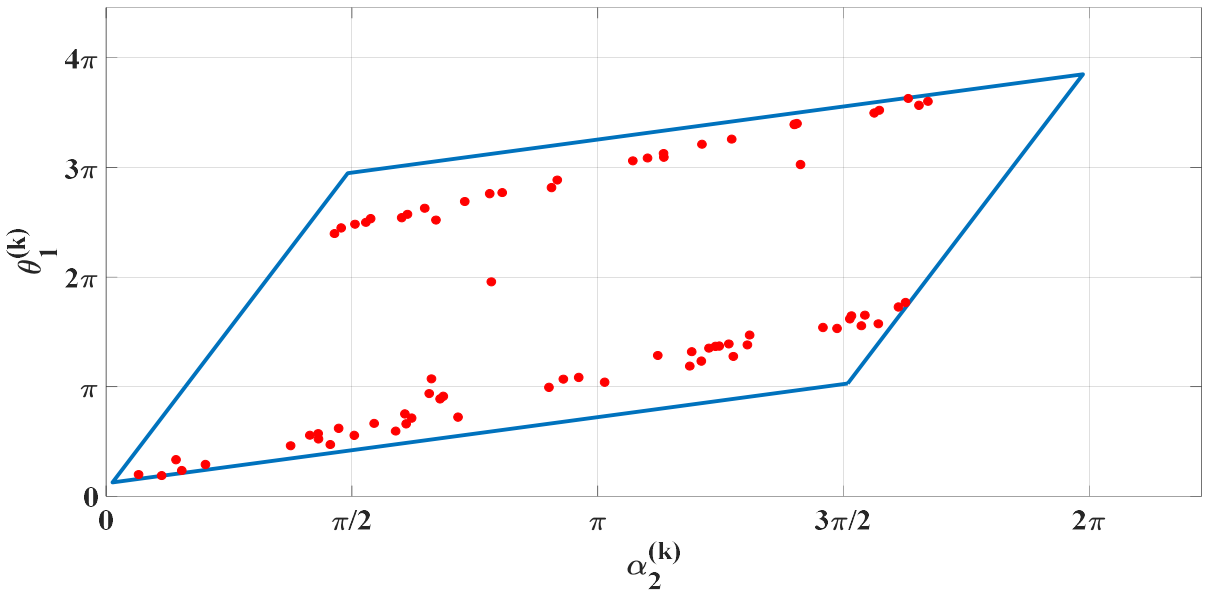

(b) $\left(\alpha_2^{(k)},\theta_1^{(k)}\right)$ at $\omega_k = 12.2\pi$ rad/s

Fig. 10: The samples of the FFT coefficients and the MP models of $\left(\beta_2^{(k)},\rho_1^{(k)}\right)$ and $\left(\alpha_2^{(k)},\theta_1^{(k)}\right)$ at $\omega_k = 12.2\pi$ rad/s

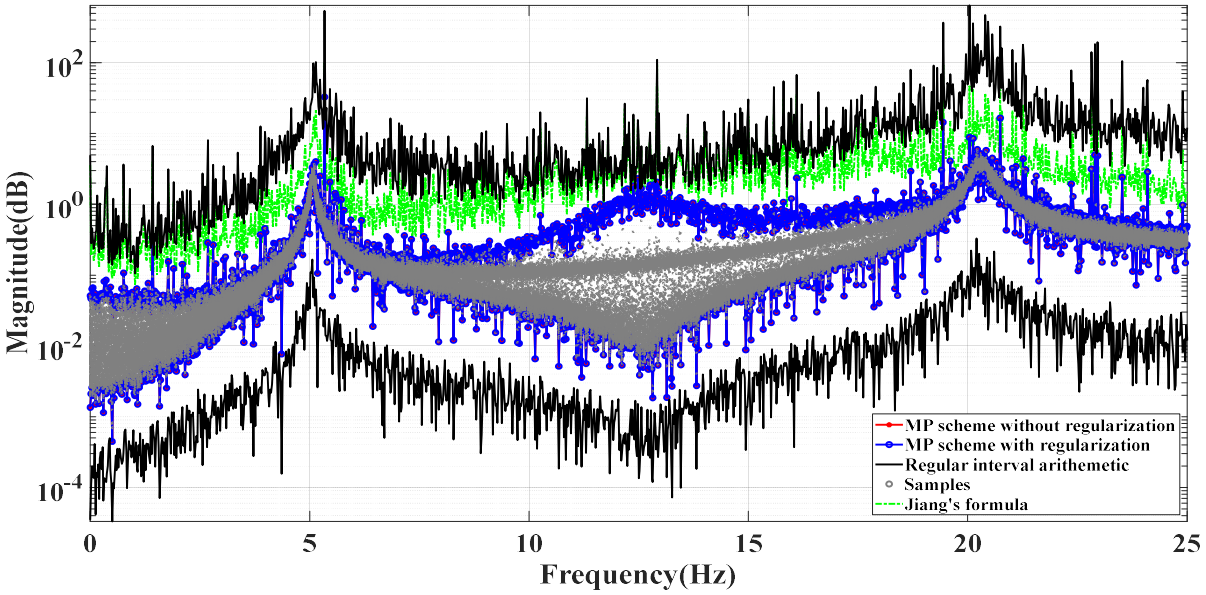

(a)

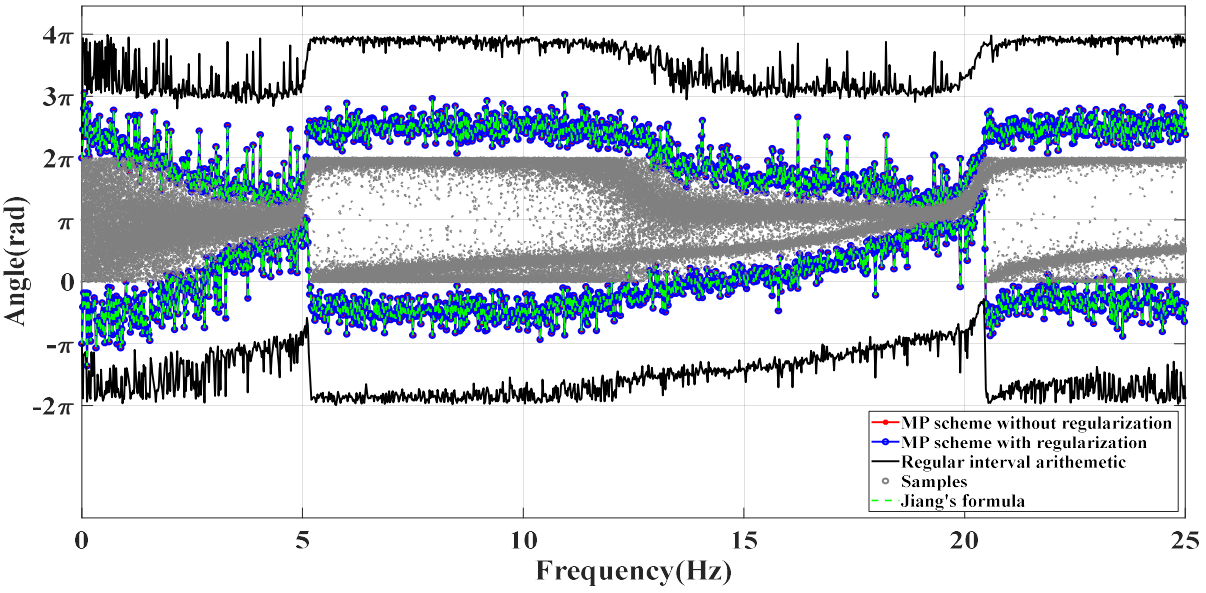

(b)

Fig. 11: The intervals of the magnitude and the angles of $H_{2,1}^{(k)}$ within *[0,25]* Hz: (a) $[\rho_1^{(k)}]/[\beta_2^{(k)}]$; (b) $[\theta_1^{(k)}]-[\alpha_2^{(k)}]$

The intervals of the TFs $T_{2,5}^{(k)}$ within *[0,25]* Hz that were produced by taking the ratio between $X_5^{(k)}$ and $X_2^{(k)}$ were also observed in detail. The parallelograms that fit the measured data at in the 2-D spaces are illustrated in Fig. 12(a) and (b). The intervals of $[\rho_5^{(k)}]/[\rho_2^{(k)}]$ that were determined by accommodating their dependence based on the MP model and without considering the dependence are compared in Fig. 13(a). The lower and upper bounds of $[\theta_5^{(k)}]-[\theta_2^{(k)}]$ that accommodated the dependence based on the MP model are compared in Fig. 13(b), along with those without consideration of the dependencies. In these figures, the results achieved by resorting to the regularization scheme and those without regularization of the uncertainty domain are denoted by red and blue dotted lines, respectively, while the results without consideration of the dependence (i.e., Eqs. (6b) and (6d)) are denoted by black solid lines.

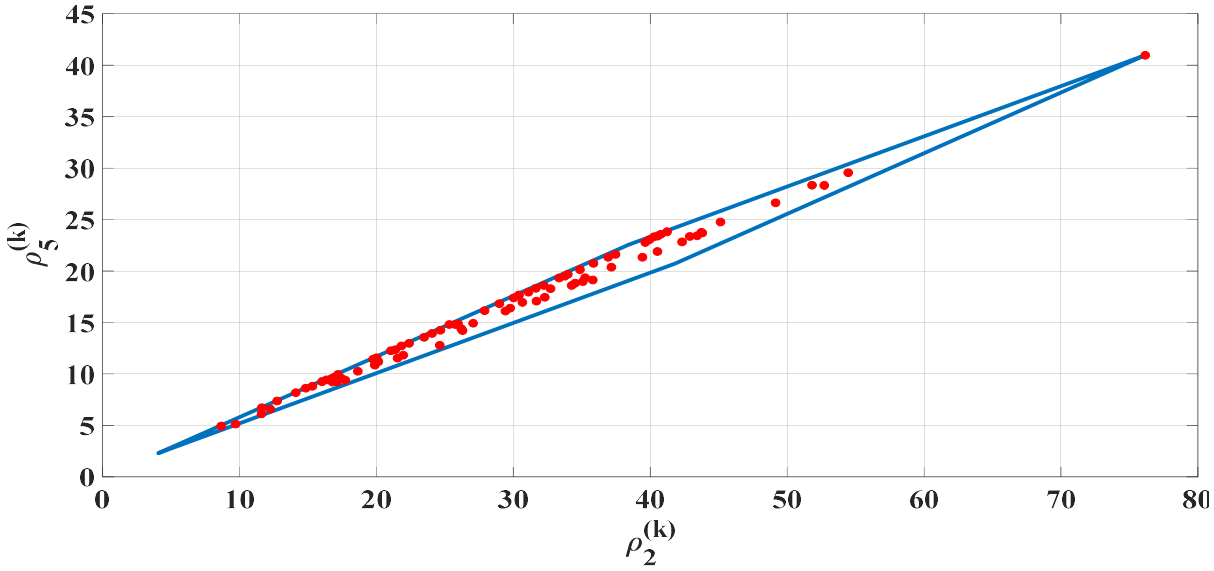

(a) $\left(\rho_5^{(k)}, \rho_2^{(k)}\right)$ at $\omega_k = 10.28\pi$ rad/s

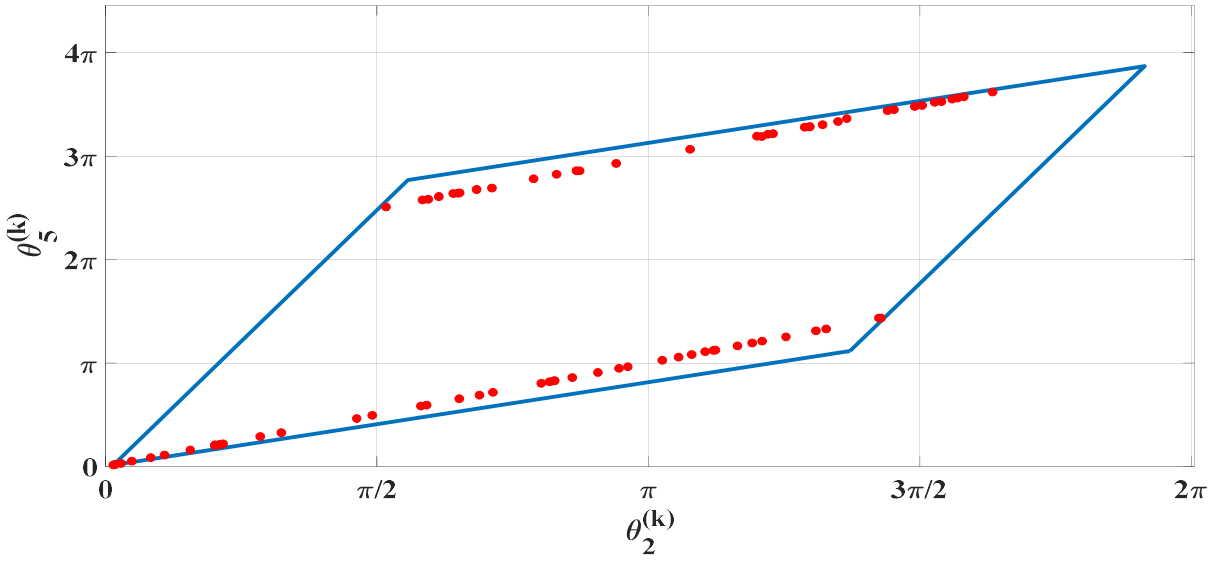

(b) $\left(\theta_5^{(k)},\theta_2^{(k)}\right)$ at $\omega_k = 10.28\pi$ rad/s

Fig. 12: The FFT samples as well as MP models of $\left(\rho_5^{(k)},\rho_2^{(k)}\right)$ and $\left(\theta_5^{(k)},\theta_2^{(k)}\right)$ at $\omega_k = 10.28\pi$ rad/s

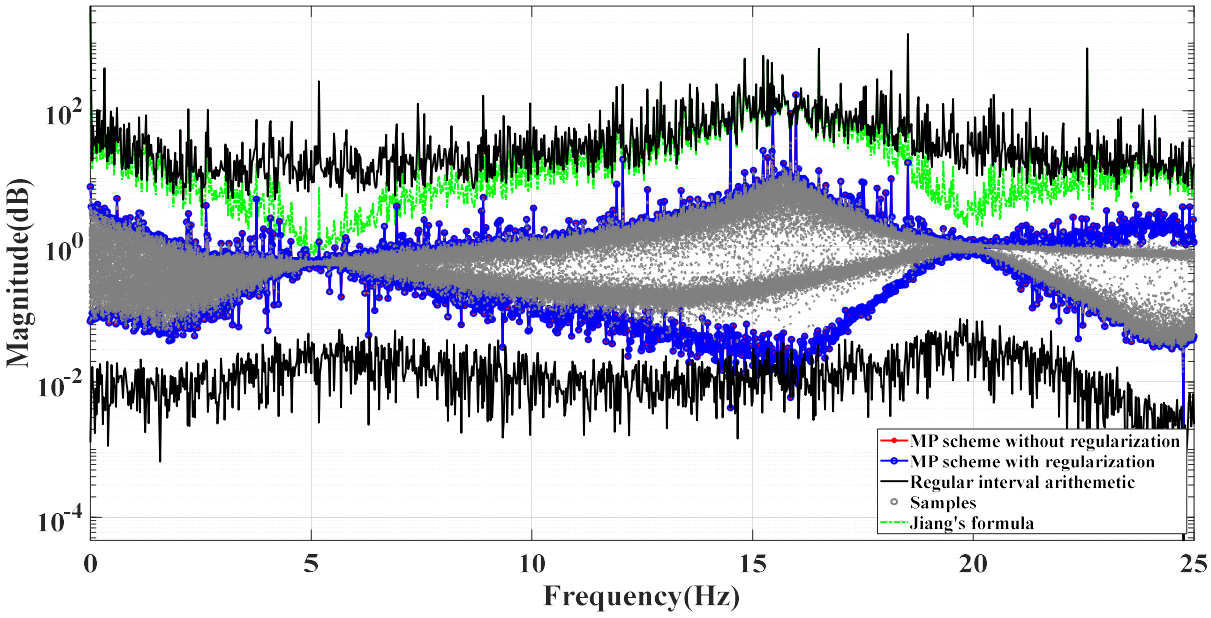

(a)

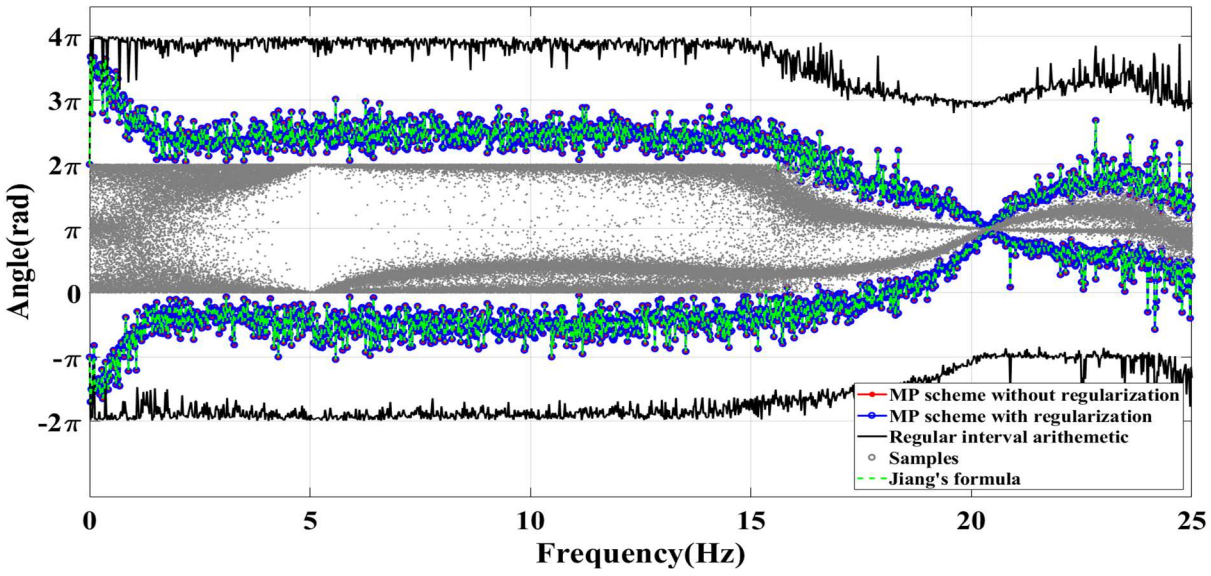

(b)

Fig. 13: The intervals of the magnitude and angles of $T_{2,5}^{(k)}$ within *[0,25]* Hz: (a) the interval of $[\rho_5^{(k)}]/[\rho_2^{(k)}]$; (b) the interval of $[\theta_5^{(k)}]-[\theta_2^{(k)}]$

Through the foregoing analysis, for either FRFs or TFs with large independence, the regular interval models were both likely to construct a too-large uncertainty domain, resulting in an ultra-conservative uncertainty quantification analysis. The parallelepiped model, however, could handle both dependent and independent variables, and it could thus be used construct a more compact uncertainty domain, resulting in more reasonable uncertainty analysis results. Furthermore, the results showed that the intervals of the magnitude obtained with Eqs. (27) and (34a) were the narrowest and they were contained in the results of the regular interval model without considering the dependences (Eq. (6d)).

6.2 Application to the uncertainty quantification of the field-testing data of a bridge

This section describes how the performance of the complex interval ratio arithmetic operations with the MP model was further evaluated by using the field test measurement for a bridge [58]. Due to the efforts of the researchers from the Los Alamos National Laboratory, the vibration

test data for a benchmark problem were available at http://ext.lanl.gov/projects/damage_id/. The bridge had seven independent spans, with each span consisting of a concrete deck supported by six steel beams. The roadway in each span was approximately 7.3-m wide and 15.2-m long. The concrete deck and the girders below the bridge were equipped with 31 sensors in total. This field test of the bridge was conducted on the bridge to study various issues related to bridge structural integrity, and the plan for the inputs (driving points A and B) and outputs (accelerometers) in forced vibration testing is shown in Fig. 14 [58]. The sampling rate of the acceleration data was 128Hz. In this study, only 30 non-overlapping sequences, with each one lasting 16s, were used for interval analysis, while the remaining measurements were not used. The FFT coefficients could be calculated accordingly for each sequence. Each segment could be viewed as a random realization and one segment could be employed to obtain the upper and lower bounds of the magnitude and angle intervals.

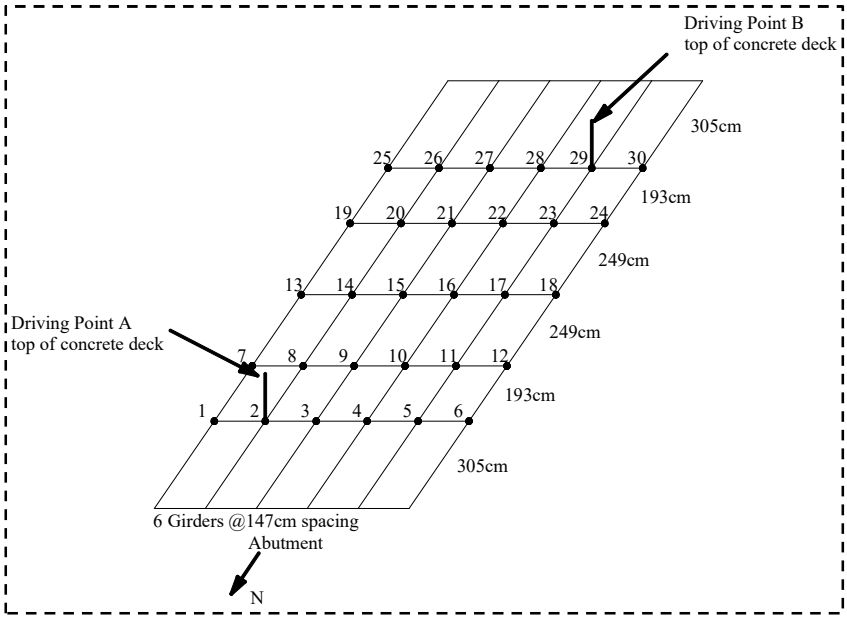

Fig. 14: Positions of the accelerometers and driving points of the bridge (redrawn according to [58])

The uncertainty domain according to the upper and lower bounds of the magnitude and angle intervals could be determined according to the FFT samples. The 2-D parallelogram

model of the magnitudes as well as the angles could be generated by circumscribing the samples. Based on all the marginal intervals and shape coefficients, the whole uncertainty domains of the magnitudes and angles at different frequency points could be created one by one. By analyzing the measurements acquired from different sensors, the following analyses were conducted:

- **FRF** $H_{2,5}^{(k)}=X_5^{(k)}/F_2^{(k)}$ **:** The parallelograms fitting the samples of the magnitude and the angles of $H_{2,5}^{(k)}$ at $\omega_k=39.625\pi$ rad/s in the 2-D space are illustrated in Fig. 15(a) and (b). The marginal intervals were equal to $[\beta_2^{(k)}]=\left[0.487\times10^{-3},0.9109\times10^{-3}\right]$, $[\rho_5^{(k)}]=\left[0.8744\times10^{-3},1.475\times10^{-3}\right]$, $[\alpha_2^{(k)}]=[1.974,3.165]$, $[\theta_5^{(k)}]=[7.977,9.298]$. The shape coefficients of $\left(\beta_2^{(k)},\rho_5^{(k)}\right)$ and $\left(\alpha_2^{(k)},\theta_5^{(k)}\right)$ were equal to $\varphi_k=0.66$ and $\varphi_k=0.73$, respectively. The shape coefficients along the frequency band [5,25Hz] are shown in Fig. 16. The uncertainty propagation analysis results based on the aforementioned non-probabilistic convex models are shown in Fig. 17. Furthermore, Fig. 17(a) displays the intervals of the magnitude (i.e., $[\rho_5^{(k)}]/[\beta_2^{(k)}]$) computed according to Eqs. (27) and (34a), while Fig. 17(b) shows the intervals of the angles of (i.e., $[\theta_5^{(k)}]-[\alpha_2^{(k)}]$) that were achieved using Eqs. (30) and (34b).

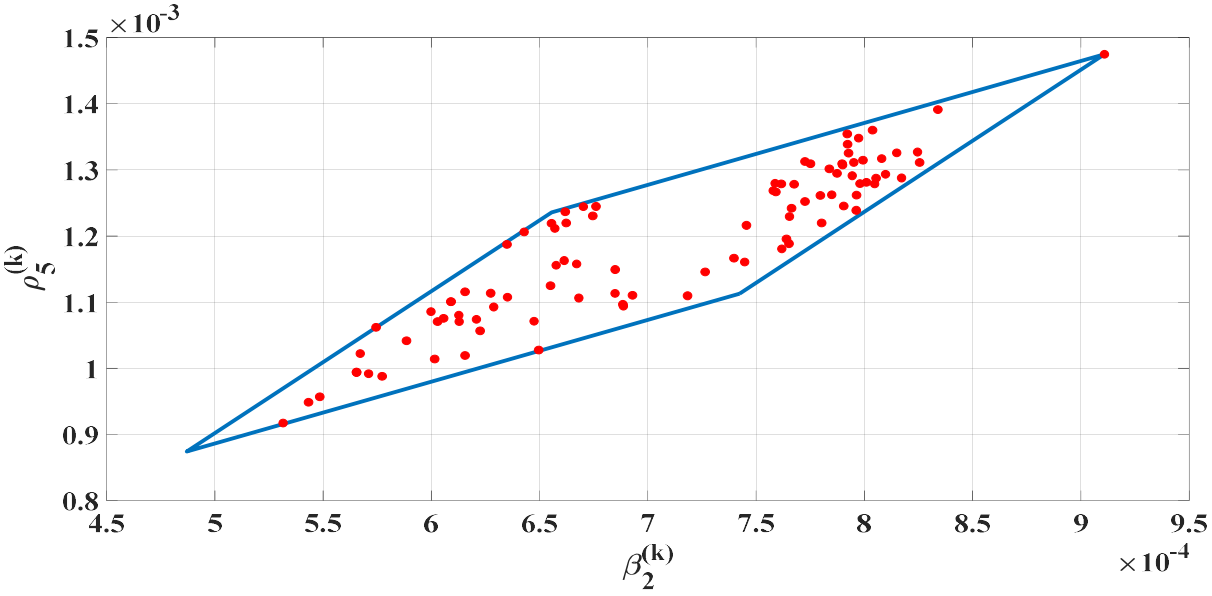

(a) $\left(\beta_2^{(k)},\rho_5^{(k)}\right)$ at $\omega_k = 39.625\pi$

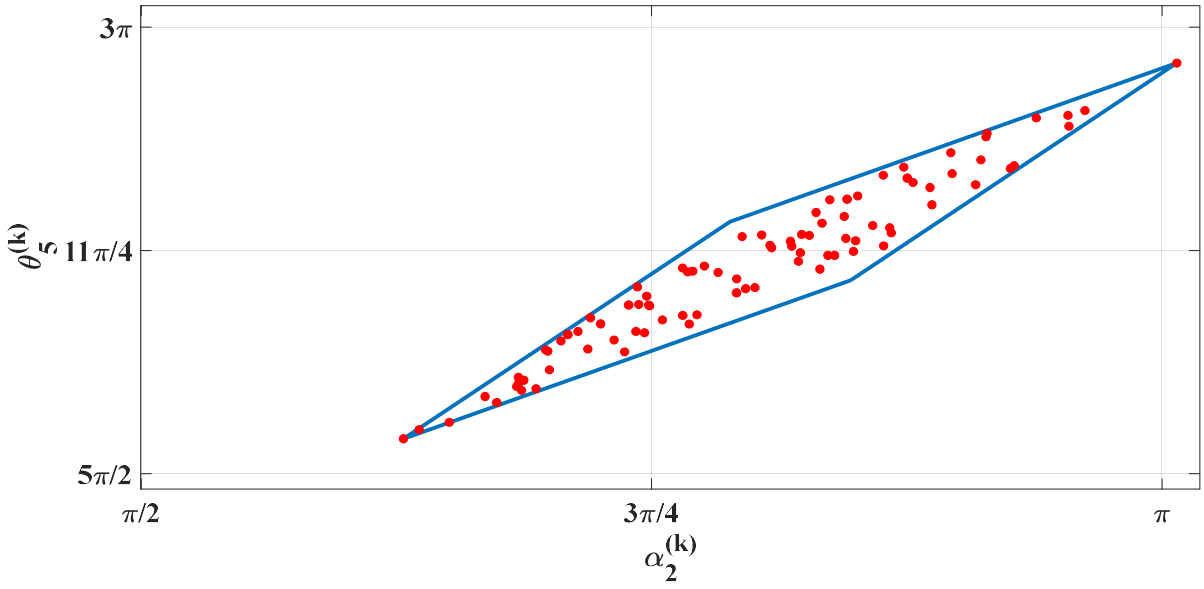

(b) $\left(\alpha_2^{(k)},\theta_5^{(k)}\right)$ at $\omega_k = 39.625\pi$ rad/s

Fig. 15: The parallelepiped models of $\left(\beta_2^{(k)},\rho_5^{(k)}\right)$ and $\left(\alpha_2^{(k)},\theta_5^{(k)}\right)$ at $\omega_k = 39.625\pi$ rad/s established based on their samples

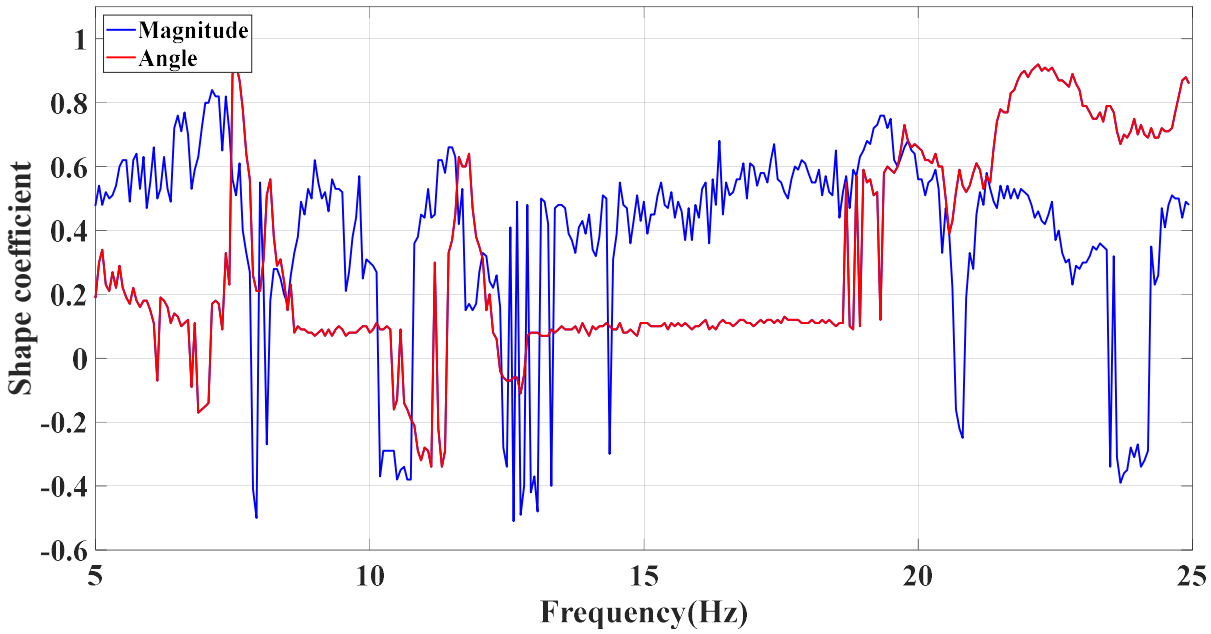

Fig. 16: The shape coefficients $\left(\beta_2^{(k)},\rho_5^{(k)}\right)$ and $\left(\alpha_2^{(k)},\theta_5^{(k)}\right)$ within the frequency band of *[5,25]* Hz

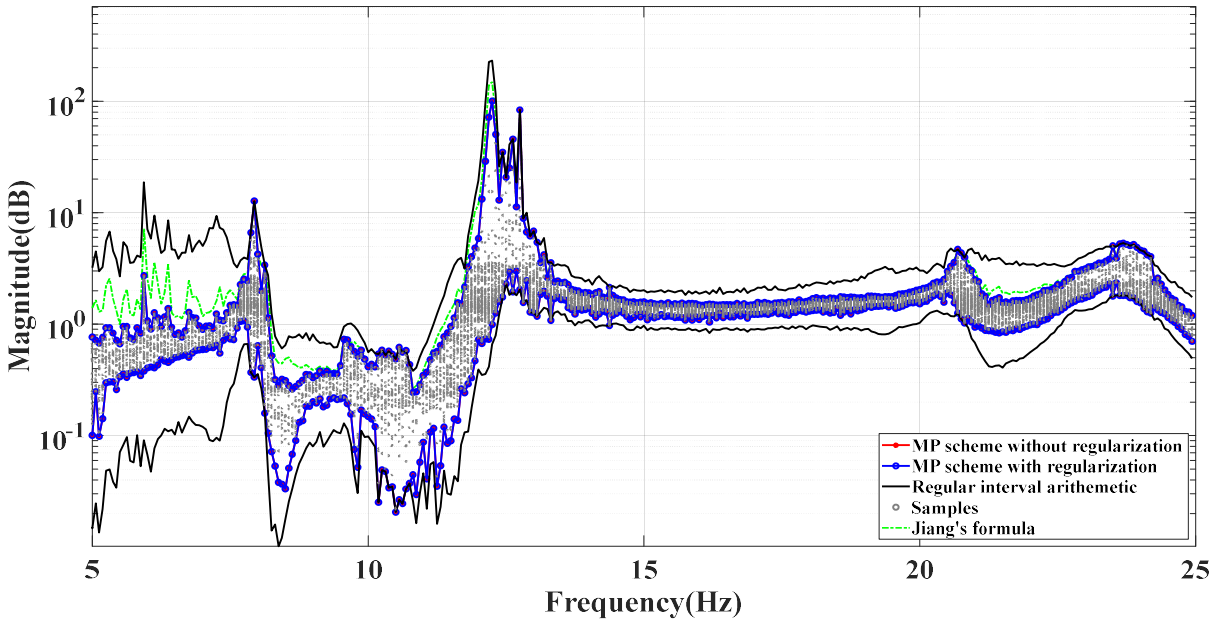

(a)

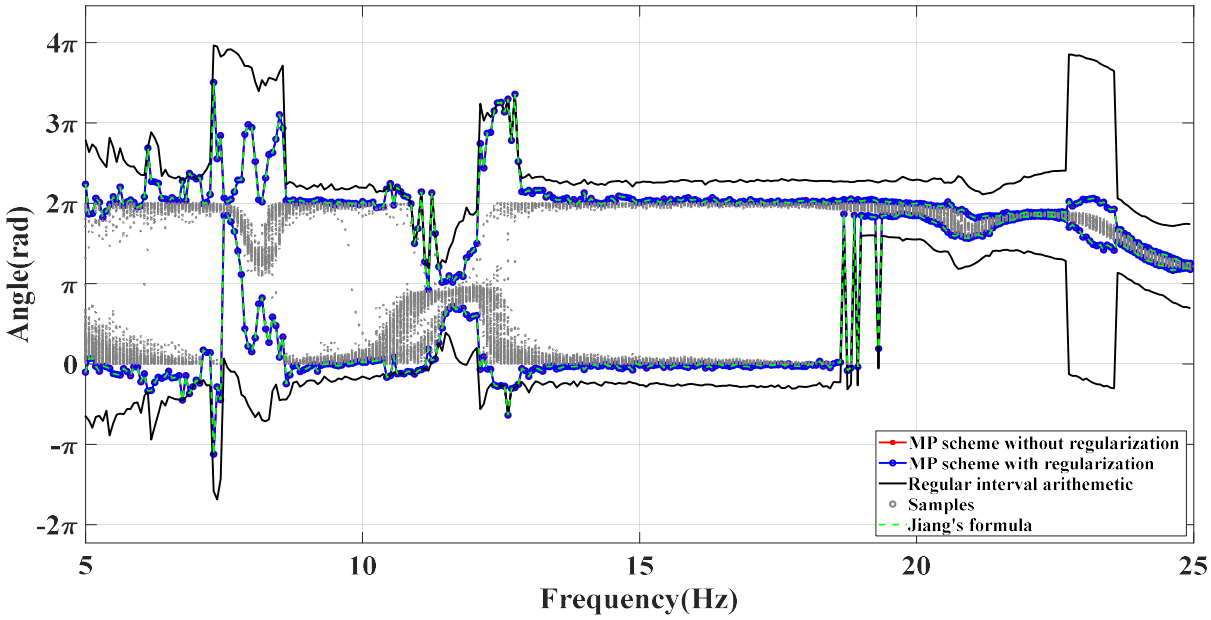

(b)

Fig. 17: The intervals of the magnitude and the angles of $H_{2,5}^{(k)}$ of the bridge within*[5,25]* Hz: (a) $[\rho_5^{(k)}]/[\beta_2^{(k)}]$; (b) $[\theta_5^{(k)}]-[\alpha_2^{(k)}]$

- **TF** $T_{1,5}^{(k)}=X_5^{(k)}/X_1^{(k)}$ **:** The parallelograms of the magnitude and angles of $T_{1,5}^{(k)}$ at $\omega_k=39.25\pi$ in the two-dimensional spaces are illustrated in Figs. 18(a) and (b) with the fittings of the samples. The marginal intervals were equal to $[\rho_1^{(k)}]=\left[0.8899\times10^{-3},1.531\times10^{-3}\right]$, $[\rho_5^{(k)}]=\left[0.753\times10^{-3},1.288\times10^{-3}\right]$, $[\theta_1^{(k)}]=[1.74,2.953]$ and $[\theta_5^{(k)}]=[1.88,3.042]$, while the shape coefficient of $\left(\rho_1^{(k)},\rho_5^{(k)}\right)$ was equal to $\varphi=0.89$ and that of $\left(\theta_1^{(k)},\theta_5^{(k)}\right)$ was equal to $\varphi=0.90$. The shape coefficients along the frequency band *[5,25]* Hz are shown in Fig. 19. The intervals of the magnitude ($[\rho_5^{(k)}]/[\rho_1^{(k)}]$) that were achieved using different schemes are displayed in Fig. 20(a), while the intervals of the angles ($[\theta_5^{(k)}]-[\theta_1^{(k)}]$) that were computed using different schemes are shown in Fig. 20(b).

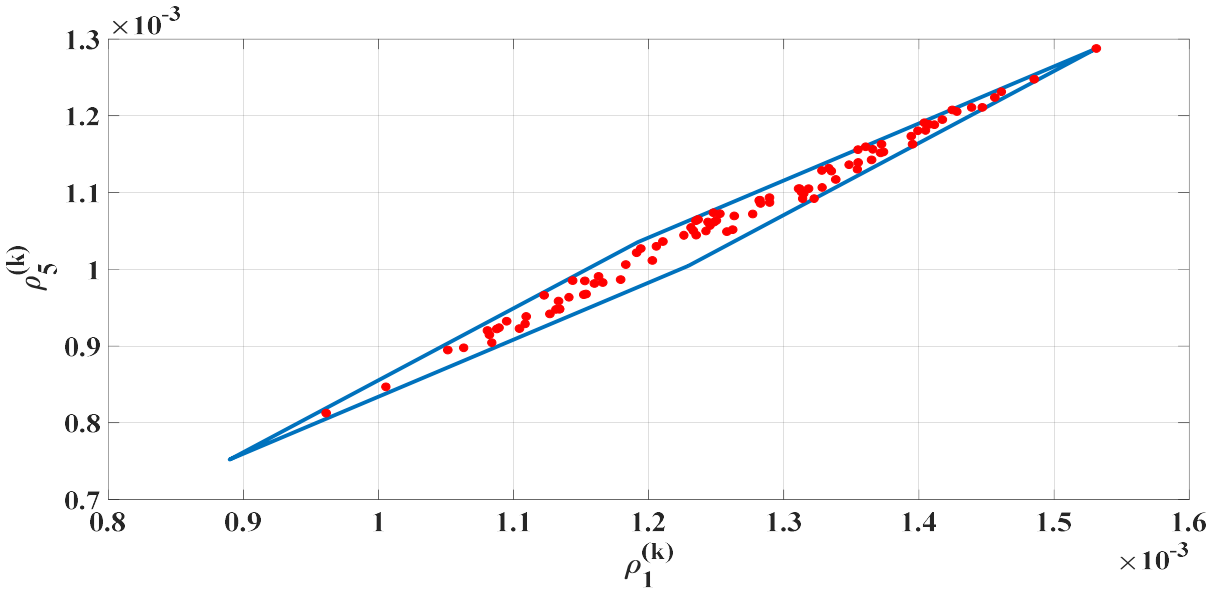

(a) $\left(\rho_1^{(k)}, \rho_5^{(k)}\right)$ at $\omega_k = 39.25\pi$ rad/s

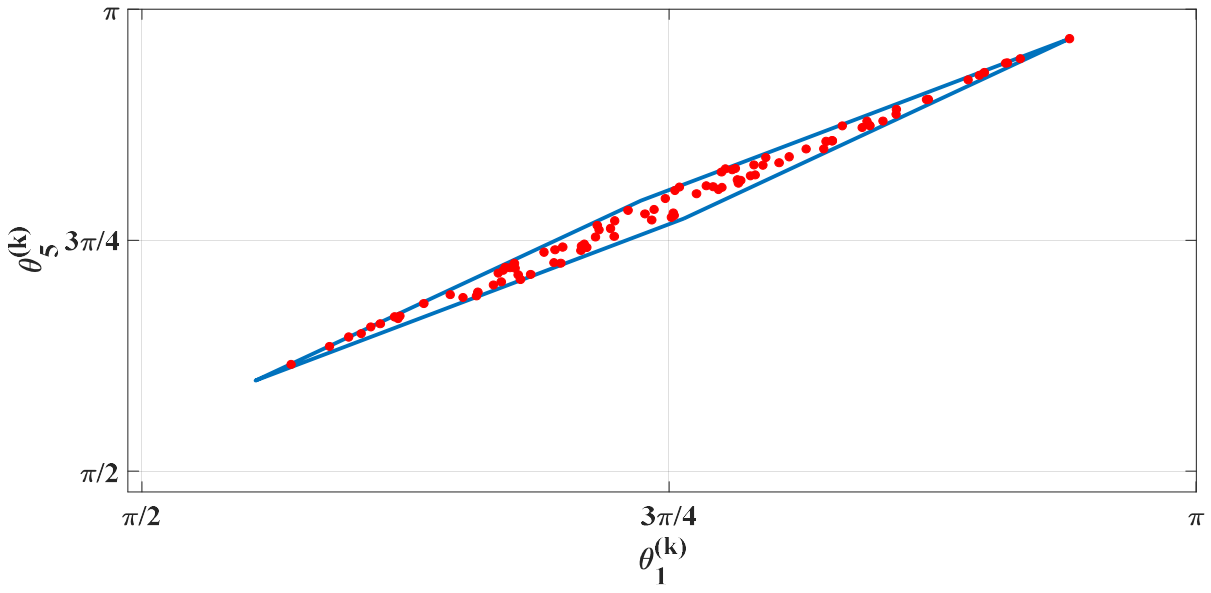

(b) $\left(\theta_1^{(k)}, \theta_5^{(k)}\right)$ at $\omega_k = 39.25\pi$ rad/s

Fig. 18: The parallelepiped models of $\left(\rho_1^{(k)}, \rho_5^{(k)}\right)$ and $\left(\theta_1^{(k)}, \theta_5^{(k)}\right)$ established based on their samples at $\omega_k = 39.25\pi$ rad/s

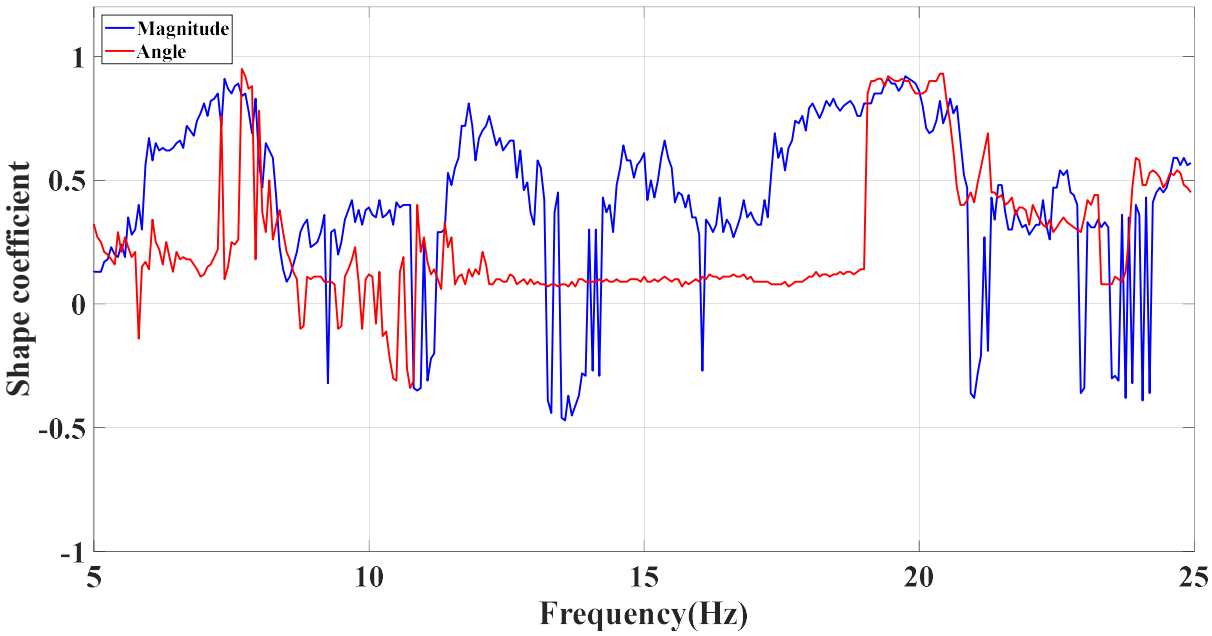

Fig. 19: The shape coefficients $\left(\rho_1^{(k)},\rho_5^{(k)}\right)$ and $\left(\theta_1^{(k)},\theta_5^{(k)}\right)$ within the frequency band *[5, 25]* Hz

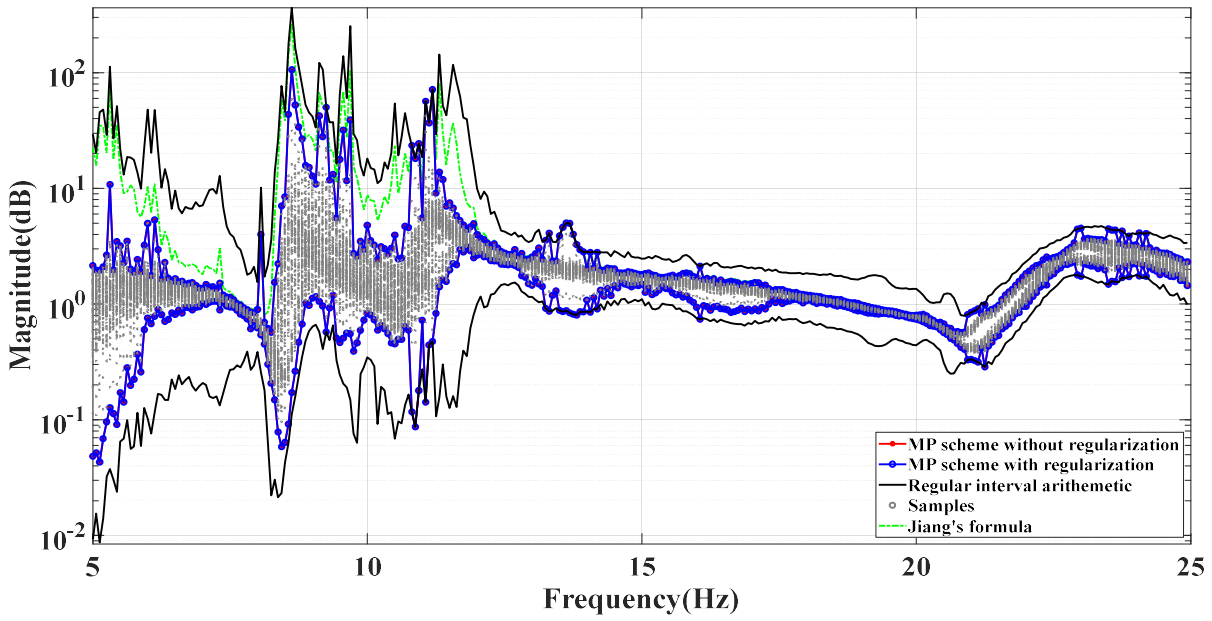

(a)

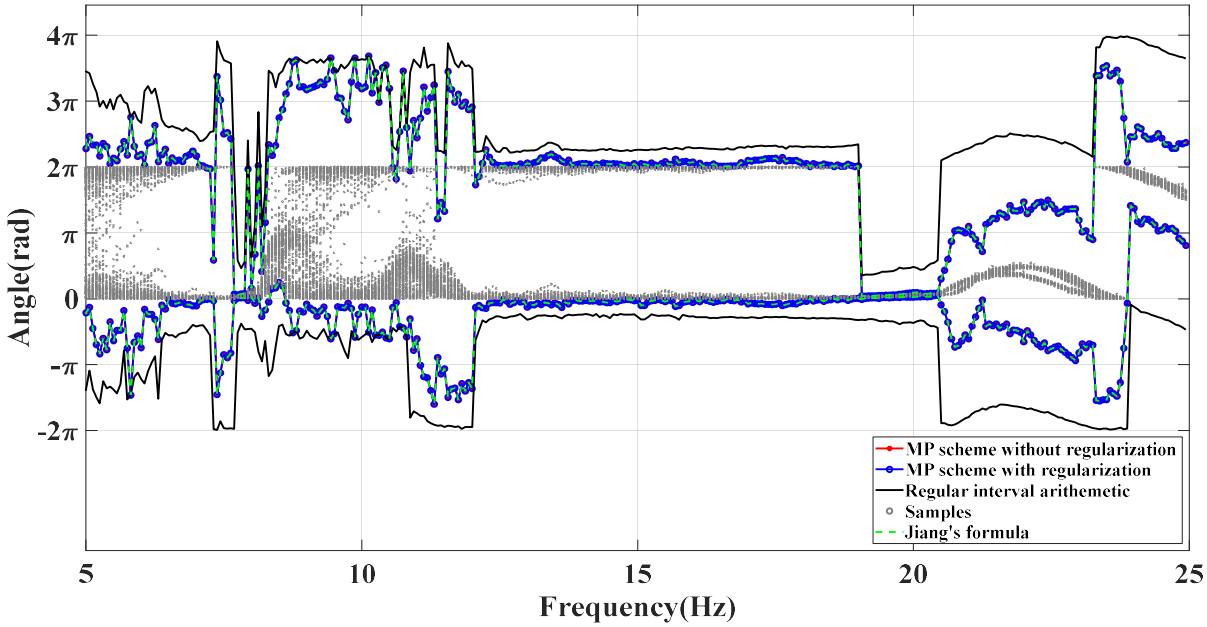

(b)

Fig. 20: Intervals of the magnitude and the angles of $T_{1,5}^{(k)}$ of the bridge within *[5, 25]* Hz: (a) $[\rho_5^{(k)}]/[\rho_1^{(k)}]$; (b) $[\theta_5^{(k)}]-[\theta_1^{(k)}]$

The following conclusions could be obtained by observing Figs. 15-20:

- The dependences between each pair of magnitudes or angles for both the FRFs and TFs could not be ignored for most of the frequency points.
- The uncertainty domain obtained from the parallelepiped model was significantly narrower than that obtained with the regular interval model. Thus, proper consideration for the dependence was of vital importance in improving the robustness of applications. The calculation results were not as conservative as those produced by the regular interval models were because the parallelepiped model constructed a more compact domain of uncertainty.
- The intervals of the magnitude and angles obtained with the new schemes with or without regulating the uncertainty domain of the MP models agreed well with each other. They

were contained by the results of the regular interval model without considering the dependences.

- The multiple occurrences of δ_x and δ_y in the division (i.e., (22a)) were regarded as multiple independent variables, which would result in interval overestimation. The interval arithmetic that was transformed to compute the maximum and the minimum of $f\left(\delta_x,\delta_y\right)$ could alleviate the interval expansion effectively.
- Fig.20(b) shows some over-conservative approximation of the phase angles, in particular for larger frequencies. However, this over-estimation is acceptable since the influence of the phase angles on the results of our approach is negligible. Further, since all angles are defined modulo 2π, results for angles greater than 2π are irrelevant. As is shown in Eqs.(7), (10) and (35), they are determined by the results from the interval [0,2π].

7 Conclusion

A new non-probabilistic approach was developed for complex-valued ratio interval arithmetic. This approach was then applied to the uncertainty quantification for the FRFs and TFs. To avoid the complexity of the rectangular representation, the polar representation of the complex ratio numbers was extended to the complex ratio polar intervals. To avoid the interval overestimation problem due to the negligence of the dependencies of the complex-valued variables, an MP interval model was introduced to accommodate the dependence between the numerator and the denominator. Based on the explicit expressions of the MP model with a dependence matrix, two global extrema searching schemes with and without regularization of the uncertainty domain of the MP model were proposed to solve the complex-valued interval ratio arithmetic. The upper and lower bounds of the magnitudes and phases of the FRFs and TFs were determined using explicit expressions. The theoretical findings of this study were

verified using the synthesis data for a simply supported beam and the forced vibration testing data for a bridge. The results showed that the intervals obtained using the new schemes proposed in this study were the narrowest and that these intervals were contained in the results of the regular interval model without considering the dependences. This development enlarged the capabilities of the FRFs and TFs with the expectation of robust analyses in the areas of inverse problems such as modal analysis, damage detection, and model updating.

Acknowledgement

This research has been supported by the Natural Science Foundation of China under Award No. 51778203, the Science and Technology Development Fund, Macau SAR (File no. FDCT/0017/2020/A1 and SKL-IOTSC-2018-2020), the Start-up Research Grant of University of Macau (File No. SRG2019-00194-IOTSC) and the Research Committee of University of Macau under Research Grant (File no.: MYRG2018-00048-AAO).

Appendix A:

Let $[x]=[\underline{x},\overline{x}]$ and $[y]=[\underline{y},\overline{y}]$ be real compact intervals; $\circ$ be one of the basic operations 'addition', 'subtraction', 'multiplication' and 'division', respectively, for real numbers, that is $\circ\in[/;-]$. Then we have the corresponding operations for intervals $[x]\circ[y]$:

$$[x]\circ[y]=\left[\min(x\circ y),\max(x\circ y)\right] \tag{A1}$$

Fig. 9 can be decomposed into three areas, i.e., Area (1), Area (2) and Area (3), and one can search the minimum and maximum values of the MP model as follows:

(1) Subtraction

For $\varphi>0$, the range of $y-x$ is given by:

- In Area (1) of Fig. 9 where $x\in[x_D,x_A]$

$$\begin{aligned}\min(y-x)&=\min\left(\left(k_1-1\right)x_D+b_1,\left(k_1-1\right)x_A+b_1\right)\\&=\min\left(y_D-x_D,y_E-x_E\right)\end{aligned}\tag{A2a}$$

$$\begin{aligned}\max(y-x)&=\max\left(\left(k_2-1\right)x_D+b_4,\left(k_2-1\right)x_A+b_4\right)\\&=\max\left(y_D-x_D,y_A-x_A\right)\end{aligned}\tag{A2b}$$

- In Area (2) of Fig. 9 where $x\in\left[x_A,x_C\right]$

$$\begin{aligned}\min(y-x)&=\min\left(\left(k_1-1\right)x_A+b_1,\left(k_1-1\right)x_C+b_1\right)\\&=\min\left(y_E-x_E,y_C-x_C\right)\end{aligned}\tag{A3a}$$

$$\begin{aligned}\max(y-x)&=\max\left(\left(k_1-1\right)x_A+b_2,\left(k_1-1\right)x_C+b_2\right)\\&=\max\left(y_A-x_A,y_F-x_F\right)\end{aligned}\tag{A3b}$$

- For Area (3) of Fig. 9 where $x\in\left[x_C,x_B\right]$

$$\begin{aligned}\min(y-x)&=\min\left(\left(k_2-1\right)x_C+b_3,\left(k_2-1\right)x_B+b_3\right)\\&=\min\left(y_C-x_C,y_B-x_B\right)\end{aligned}\tag{A4a}$$

$$\begin{aligned}\max(y-x)&=\min\left(\left(k_1-1\right)x_C+b_2,\left(k_1-1\right)x_B+b_2\right)\\&=\min\left(y_F-x_F,y_B-x_B\right)\end{aligned}\tag{A4b}$$

Synthesizing the above formula, $[y]-[x]$ is equal to:

$$\begin{aligned}[y]-[x]=\big[&\min\left(y_A-x_A,y_B-x_B,y_C-x_C,y_D-x_D,y_E-x_E,y_F-x_F\right),\\&\max\left(x_A-y_A,x_B-y_B,x_C-y_C,x_D-y_D,x_E-y_E,x_F-y_F\right)\big]\end{aligned}\tag{A5}$$

It is worth noting that

$$\begin{aligned}&\min\left(y_C-x_C,y_D-x_D\right)\le y_E-x_E\le\max\left(y_C-x_C,y_D-x_D\right)\\&\min\left(y_A-x_A,y_B-x_B\right)\le y_F-x_F\le\max\left(y_A-x_A,y_B-x_B\right)\end{aligned}\tag{A6}$$

As a result, Eq.(5) reduces to

$$\begin{aligned}[y]-[x]=\big[&\min\left(y_A-x_A,y_B-x_B,y_C-x_C,y_D-x_D\right),\\&\max\left(x_A-y_A,x_B-y_B,x_C-y_C,x_D-y_D\right)\big]\end{aligned}\tag{A7}$$

For $\varphi>0$, the result of $[y]-[x]$ is completely the same as those of $\varphi>0$, and the procedures are omitted here.

(2) Division

For $\varphi>0$, the range of $\frac{y}{x}$ is given by:

- In Area (1) of Fig. 9 where $x\in\left[x_D,x_A\right]$:

$$\begin{aligned}\min\left(\frac{y}{x}\right)&=\min\left(k_1+\frac{b_1}{x_D},k_1+\frac{b_1}{x_E},k_2+\frac{b_4}{x_D},k_2+\frac{b_4}{x_A}\right)\\&=\min\left(\frac{y_D}{x_D},\frac{y_E}{x_E},\frac{y_A}{x_A}\right)\end{aligned}\tag{A8a}$$

$$\begin{aligned}\max\left(\frac{y}{x}\right)&=\max\left(k_1+\frac{b_1}{x_D},k_1+\frac{b_1}{x_E},k_2+\frac{b_4}{x_D},k_2+\frac{b_4}{x_A}\right)\\&=\max\left(\frac{y_D}{x_D},\frac{y_E}{x_E},\frac{y_A}{x_A}\right)\end{aligned}\tag{A8b}$$

- In Area (2) of Fig. 9 where where $x\in\left[x_A,x_C\right]$:

$$\begin{aligned}\min\left(\frac{y}{x}\right)&=\min\left(k_1+\frac{b_1}{x_E},k_1+\frac{b_1}{x_C},k_1+\frac{b_2}{x_A},k_1+\frac{b_2}{x_F}\right)\\&=\min\left(\frac{y_E}{x_E},\frac{y_C}{x_C},\frac{y_A}{x_A},\frac{y_F}{x_F}\right)\end{aligned}\tag{A9a}$$

$$\begin{aligned}\max\left(\frac{y}{x}\right)&=\max\left(k_1+\frac{b_1}{x_E},k_1+\frac{b_1}{x_C},k_1+\frac{b_2}{x_A},k_1+\frac{b_2}{x_F}\right)\\&=\max\left(\frac{y_E}{x_E},\frac{y_C}{x_C},\frac{y_A}{x_A},\frac{y_F}{x_F}\right)\end{aligned}\tag{A9b}$$

- For Area (3) of Fig. 9 where $x\in\left[x_C,x_B\right]$:

$$\begin{aligned}\min\left(\frac{y}{x}\right)&=\min\left(k_2+\frac{b_3}{x_C},k_2+\frac{b_3}{x_B},k_1+\frac{b_2}{x_F},k_1+\frac{b_2}{x_B}\right)\\&=\min\left(\frac{y_C}{x_C},\frac{y_B}{x_B},\frac{y_F}{x_F}\right)\end{aligned}\tag{A10a}$$

$$\begin{aligned}\max\left(\frac{y}{x}\right)&=\max\left(k_2+\frac{b_3}{x_C},k_2+\frac{b_3}{x_B},k_1+\frac{b_2}{x_F},k_1+\frac{b_2}{x_B}\right)\\&=\max\left(\frac{y_C}{x_C},\frac{y_B}{x_B},\frac{y_F}{x_F}\right)\end{aligned}\tag{A10b}$$

Synthesizing the above formula for $\varphi>0$, $\frac{[y]}{[x]}$ is equal to:

$$\frac{[y]}{[x]}=\left[\min\left(\frac{y_A}{x_A},\frac{y_B}{x_B},\frac{y_C}{x_C},\frac{y_D}{x_D},\frac{y_E}{x_E},\frac{y_F}{x_F}\right),\max\left(\frac{y_A}{x_A},\frac{y_B}{x_B},\frac{y_C}{x_C},\frac{y_D}{x_D},\frac{y_E}{x_E},\frac{y_F}{x_F}\right)\right] \tag{A11}$$

It is worth noting that

$$\begin{aligned}\min\left(\frac{y_C}{x_C},\frac{y_D}{x_D}\right)\le\frac{y_E}{x_E}\le\max\left(\frac{y_C}{x_C},\frac{y_D}{x_D}\right)\\ \min\left(\frac{y_A}{x_A},\frac{y_B}{x_B}\right)\le\frac{y_F}{x_F}\le\max\left(\frac{y_A}{x_A},\frac{y_B}{x_B}\right)\end{aligned} \tag{A12}$$

As a result, Eq.(A11) can be simplified as

$$\frac{[y]}{[x]}=\left[\min\left(\frac{y_A}{x_A},\frac{y_B}{x_B},\frac{y_C}{x_C},\frac{y_D}{x_D}\right),\max\left(\frac{y_A}{x_A},\frac{y_B}{x_B},\frac{y_C}{x_C},\frac{y_D}{x_D}\right)\right] \tag{A13}$$

For $\varphi<0$, the formula is completely the same as those of $\varphi>0$, thus the procedures are omitted here for the purpose of simplicity.

Reference

[1] J. Antoni, Leakage-free identification of FRF's with the discrete time Fourier transform, Journal of Sound and Vibration, 294(4) (2006) 981-1003.

[2] L. Jiang, Y. Feng, W. Zhou, B. He, Vibration characteristic analysis of high-speed railway simply supported beam bridge-track structure system, Steel and Composite Structures, 31(6) (2019) 591-600.

[3] D.E. Adams, Frequency domain ARX model and multi-harmonic FRF estimators for non-linear dynamic systems, Journal of Sound and Vibration, 250 (5) (2002) 935-950.

[4] W.J. Yan, M.Y. Zhao, Q. Sun, et al, Transmissibility-based system identification for structural health monitoring: Fundamentals, approaches, and applications, Mechanical Systems and Signal Processing, 117 (2019) 453-482.

[5] N.M.M. Maia, R. Almeida, A.P.V. Urgueira, R.P.C. Sampaio, Damage detection and quantification using transmissibility, Mechanical Systems and Signal Processing, 25 (7) (2011) 2475-2483.

[6] K. Worden, Structural fault detection using a novelty measure, Journal of Sound and Vibration, 201 (1) (1997) 85-101.

[7] C. Simon, D. Arnaud, Damage localization using transmissibility functions: A critical review, Mechanical Systems and Signal Processing, 38 (2) (2013) 569-584.

[8] C. Devriendt, P. Guillaume, The use of transmissibility measurements in output-only modal analysis, Mechanical Systems and Signal Processing, 21 (7) (2007) 2689-2696.

[9] W.J. Yan, W.X. Ren, Operational modal parameter identification from power spectrum density transmissibility, Computer-Aided Civil and Infrastructure Engineering, 27 (3) (2012) 202-217.

[10] W.J. Yan, W.X. Ren, An Enhanced Power Spectral Density Transmissibility (EPSDT) approach for operational modal analysis: Theoretical and experimental investigation, Engineering Structures, 102 (2015) 108-119.

[11] V. Meruane, Model updating using antiresonant frequencies identified from transmissibility functions, Journal of Sound and Vibration, 332 (4) (2013) 807-820.

[12] K.V. Yuen, L.S. Katafygiotis, Model updating using response measurements without knowledge of the input spectrum, Earthquake Engineering and Structural Dynamics, 34 (2) (2005) 167-187.

[13] S.S. Law, J. Li, Y. Ding, Structural response reconstruction with transmissibility concept in frequency domain, Mechanical Systems and Signal Processing, 25 (3) (2011) 952-968.

[14] H.P. Zhu, L. Mao, S. Weng, A sensitivity-based structural damage identification method with unknown input excitation using transmissibility concept, Journal of Sound and Vibration, 333 (26) (2014) 7135-7150.

[15] Z. Xiao, X.J. Jing, L. Cheng, The transmissibility of vibration isolators with cubic nonlinear damping under both force and base excitations, Journal of Sound and Vibration, 332 (5) (2013) 1335-1354.

[16] R. Pintelon, P. Guillaume, Y. Rolain, J. Schoukens, H.V. Hamme, Parametric identification of transfer functions in the frequency domain: a survey, IEEE Transactions on Automatic Control, 39 (11) (1994) 2245-2260.

[17] C. Devriendt, P. Guillaume, Identification of modal parameters from transmissibility measurements, Journal of Sound and Vibration, 314 (1-2) (2008) 343-356.

[18] W.J. Yan, M.Y. Zhao, M. Beer, W.X. Ren, and D. Chronopoulos, A unified scheme to solving arbitrary complex-valued ratio distribution with application to statistical inference for raw frequency response functions and transmissibility functions, Mechanical Systems and Signal Processing, 145 (2020) 106886.

[19] B. Möller, M. Beer, Fuzzy Randomness: Uncertainty in Civil Engineering and Computational Mechanics, Springer Science & Business Media, 2004.

[20] J.B. Chen, J. Li, Dynamic response and reliability analysis of non-linear stochastic structures, Probabilistic Engineering Mechanics, 20(1) (2005) 33-44.

[21] R. Pintelon, Y. Rolain, W. Van Moer, Probability density function for frequency response function measurements using periodic signals, IEEE Transactions on Instrumentation and Measurement, 52 (1) (2003) 61-68.

[22] Z. Mao, M.D. Todd, Statistical modeling of frequency response function estimation for uncertainty quantification, Mechanical Systems and Signal Processing, 38 (2) (2013) 333-345.

[23] W.J. Yan, W.X. Ren, Generalized proper complex Gaussian ratio distribution and its application to statistical inference for frequency response functions, Journal of Engineering Mechanics, 144 (9) (2018) 04018080.

[24] Z. Mao, M.D. Todd, A model for quantifying uncertainty in the estimation of noise-contaminated measurements of transmissibility, Mechanical Systems and Signal Processing, 28 (2012) 470-481.

[25] W.J. Yan, W.X. Ren, Circularly-symmetric complex normal ratio distribution for scalar transmissibility function. Part I: Fundamentals, Mechanical Systems and Signal Processing, 80 (2016) 58-77.

[26] W.J. Yan, W.X. Ren, Circularly-symmetric complex normal ratio distribution for scalar transmissibility function. Part II: Probabilistic model and validation, Mechanical Systems and Signal Processing, 80 (2016) 78-98.

[27] I. Elishakoff, Possible limitations of probabilistic methods in engineering, Applied Mechanics Reviews (ASME), 53(2) (2000) 19-36.

[28] M. Faes, M. Broggi, E. Patelli, Y. Govers, J. Mottershead, M. Beer, D. Moens, A multivariate interval approach for inverse uncertainty quantification with limited experimental data, Mechanical Systems and Signal Processing, 118 (2019) 534-548.

[29] M. Imholz, M. Faes, D. Vandepitte, D. Moens, Robust uncertainty quantification in structural dynamics under scarse experimental modal data: A Bayesian-interval approach. Journal of Sound and Vibration, 467 (2020) 114983.

[30] M. Faes, D. Moens, Recent trends in the modeling and quantification of non-probabilistic uncertainty, Archives of Computational Methods in Engineering (2019) 1-39.

[31] W.J. Yan, L. Yang, X. Yang, W.X. Ren, Statistical modeling for fast Fourier transform coefficients of operational vibration measurements with non-Gaussianity using complex-valued t distribution, Mechanical Systems and Signal Processing, 132 (2019) 293-314.

[32] W. Gao, Interval natural frequency and mode shape analysis for truss structures with interval parameters, Finite Elements in Analysis and Design, 42(6) (2006) 471-477.

[33] Z. Qiu, X. Wang, M.I. Friswell, Eigenvalue bounds of structures with uncertain-but-bounded parameters, Journal of Sound and Vibration, 282(1-2) (2005) 297-312.

[34] D. Moens, D. Vandepitte, An interval finite element approach for the calculation of envelope frequency response functions, International Journal for Numerical Methods in Engineering, 61 (14) (2004) 2480-2507.

[35] D. Moens, D. Vandepitte, A fuzzy finite element procedure for the calculation of uncertain frequency response functions of damped structures: Part 1-procedure, Journal of Sound and Vibration, 288 (3) (2005) 431-462.

[36] D. Moens, D. Vandepitte, Interval sensitivity theory and its application to frequency response envelope analysis of uncertain structures, Computer methods in applied mechanics and engineering, 196(21-24) (2007) 2486-2496.

[37] C. Xiong, L. Wang, G.H. Liu, Q.H. Shi, An iterative dimension-by dimension method for structural interval response prediction with multidimensional uncertain variables, Aerospace Science and Technology, 86 (2019) 572-581.

[38] X.X. Liu, I. Elishakoff, A combined importance sampling and active learning Kriging reliability method for small failure probability with random and correlated interval variables, Structural Safety, 82 (2020) 101875.

[39] C. Wang, H. Zhang, M. Beer, Computing tight bounds of structural reliability under imprecise probabilistic information, Computers & Structures, 208 (2018) 92-104.

[40] L. Wang, X.J. Wang, Y.L. Li, J.X. Hu, A non-probabilistic time-variant reliable control method for structural vibration suppression problems with interval uncertainties, Mechanical Systems and Signal Processing, 115 (2019) 301-322.

[41] H.H. Khodaparast, J.E. Mottershead, K.J. Badcock, Interval model updating with irreducible uncertainty using the Kriging predictor, Mechanical Systems and Signal Processing, 25 (4) (2011) 1204-1226.

[42] L. Wang, Y.R. Liu, Y.S. Liu, An inverse method for distributed dynamic load identification of structures with interval uncertainties, Advances in Engineering Software, 131 (2019) 77-89.

[43] L. Wang, Y. Liu, A novel method of distributed dynamic load identification for aircraft structure considering multi-source uncertainties, Structural and Multidisciplinary Optimization, 61 (2020) 1929-1952.

[44] J. Rokne, P. Lancaster, Complex interval arithmetic, Communications of the ACM, 14 (2) (1971) 111-112

[45] R. Lohner, J. Wolff, V. Gudenberg, Complex interval division with maximum accuracy, IEEE 7th Symposium on Computer Arithmetic, 1985, 332-336.

[46] C. Jiang, X. Han, G.Y. Lu, J. Liu, Z. Zhang, Y.C. Bai, Correlation analysis of non-

probabilistic convex model and corresponding structural reliability technique, Computer Methods in Applied Mechanics and Engineering, 200 (33-36) (2011) 2528-2546

[47] C. Jiang, Q.F. Zhang, X. Han, Multidimensional parallelepiped model-a new type of non-probabilistic convex model for structural uncertainty analysis, International Journal for Numerical Methods in Engineering, 103 (1) (2015) 31-59.

[48] M. Faes, D. Moens, Multivariate dependent interval finite element analysis via convex hull pair constructions and the extended transformation method, Computer Methods in Applied Mechanics and Engineering, 347 (2019) 85-102.

[49] Y. Candau, T. Raissi, N. Ramdani, Complex interval arithmetic using polar form, Reliable Computing, 12 (2006) 1-20.

[50] B.Y. Ni, C. Jiang, X. Han, An improved multidimensional parallelepiped non-probabilistic model for structural uncertainty analysis, Applied Mathematical Modelling, 40 (7-8) (2016) 4727-4745.

[51] C. Jiang, C.M. Fu, B.Y. Ni, X. Han, Interval arithmetic operations for uncertainty analysis with correlated interval variables, Acta Mechanica Sinica, 32 (4) (2015) 743-752.

[52] K.V. Yuen, L.S. Katafygiotis, J.L. Beck, Spectral density estimation of stochastic vector processes, Probabilistic Engineering Mechanics, 17 (3) (2002) 265-272.

[53] K.V. Yuen, L.S. Katafygiotis, Bayesian fast Fourier transform approach for modal updating using ambient data, Advance in Structural Engineering 6(2) (2003) 81-95.

[54] K.V. Yuen, Bayesian Methods for Structural Dynamics and Civil Engineering, John Wiley & Sons Ltd, New York, 2010.

[55] W.J. Yan, D. Chronopoulos, S. Cantero-Chinchilla, K.V. Yuen, C. Papadimitriou, A fast Bayesian inference scheme for identification of local structural properties of layered composites based on wave and finite element-assisted metamodeling strategy and ultrasound measurements, Mechanical Systems and Signal Processing, 143(2020) 106802.

[56] I. Elishakoff, N. Sarlin, Uncertainty quantification based on pillars of experiment, theory, and computation, Part I: Data analysis, Mechanical Systems and Signal Processing, 74 (2016) 29-53.

[57] D. Degrauwe, G. Lombaert, G. De Roeck, Improving interval analysis in finite element calculations by means of affine arithmetic, Computers & structures, 88(3-4) (2010) 247-254.

[58] C. R. Farrar, P. J. Cornwell, S. W. Doebling, M. B. Prime, Structural health monitoring studies of the Alamosa canyon and I-40 Bridges. Los Alamos National Laboratory report, LA-13635-MS, 2000.